CALCIUM SIGNALING

ER-mitochondria cross-talk is regulated by the Ca^{2+} sensor NCS1 and is impaired in Wolfram syndrome

Claire Angebault[1,2]*, Jérémy Fauconnier[2]*, Simone Patergnani[3,4], Jennifer Rieusset[5], Alberto Danese[3], Corentin A. Affortit[1], Jolanta Jagodzinska[1], Camille Mégy[1], Mélanie Quiles[1], Chantal Cazevieille[1], Julia Korchagina[1], Delphine Bonnet-Wersinger[1], Dan Milea[6,7], Christian Hamel[1,8†], Paolo Pinton[3], Marc Thiry[9], Alain Lacampagne[2], Benjamin Delprat[1,10‡§], Cécile Delettre[1‡§]

Communication between the endoplasmic reticulum (ER) and mitochondria plays a pivotal role in Ca^{2+} signaling, energy metabolism, and cell survival. Dysfunction in this cross-talk leads to metabolic and neurodegenerative diseases. Wolfram syndrome is a fatal neurodegenerative disease caused by mutations in the ER-resident protein WFS1. Here, we showed that WFS1 formed a complex with neuronal calcium sensor 1 (NCS1) and inositol 1,4,5-trisphosphate receptor (IP_3R) to promote Ca^{2+} transfer between the ER and mitochondria. In addition, we found that NCS1 abundance was reduced in WFS1-null patient fibroblasts, which showed reduced ER-mitochondria interactions and Ca^{2+} exchange. Moreover, in WFS1-deficient cells, NCS1 overexpression not only restored ER-mitochondria interactions and Ca^{2+} transfer but also rescued mitochondrial dysfunction. Our results describe a key role of NCS1 in ER-mitochondria cross-talk, uncover a pathogenic mechanism for Wolfram syndrome, and potentially reveal insights into the pathogenesis of other neurodegenerative diseases.

INTRODUCTION

Mitochondria play a role in various essential cellular functions, including bioenergetics, metabolism, ion homeostasis, and apoptosis. Mitochondrial dysfunction has been linked to many common neurodegenerative disorders that are disabling and are often fatal. However, the cause of mitochondrial dysfunction remains largely undefined. Mitochondria interact physically and functionally with endoplasmic reticulum (ER) through mitochondria-associated membranes (MAMs) (*1*–*3*) to influence cellular physiology and viability (*4*, *5*). Accordingly, impaired MAM function is increasingly recognized as a contributor to neurodegeneration (*6*, *7*).

Loss of function of the ER protein WFS1 leads to a neurodegenerative disease called Wolfram syndrome that is associated with diabetes, optic atrophy, and deafness (*8*). Wolfram syndrome was originally described as a mitochondriopathy due to a clinical phenotype that resembled other mitochondrial disorders (*9*). However, this hypothesis has been challenged because WFS1 localized to the ER (*10*). A relationship between cytosolic Ca^{2+} disturbance, impaired mitochondrial dynamics, and delayed neuronal development in WFS1-deficient neurons has been suggested (*11*). Here, we report the identification of a WFS1 binding partner, neuronal calcium sensor 1 (NCS1), a cytoplasmic Ca^{2+} binding protein that is abundant in neurons. Our data suggest that NCS1 promoted ER-mitochondria contact and Ca^{2+} transfer, subsequently controlling mitochondrial bioenergetics. This study shows that WFS1 and NCS1 may participate in the tethering of ER to mitochondria and the lack of this interaction may contribute to neurodegeneration.

RESULTS

Loss of function of WFS1 does not impair mitochondrial morphology

To investigate the effect of WFS1 deficiency, we took advantage of fibroblasts from Wolfram syndrome patients, which are WFS1 null. The patients carried predicted loss-of-function alleles in *WFS1* (patients 1 and 2, V509-Y513del and F882fsX950; patient 3, homozygous for L432V; patient 4, c.1-43G>T and W867X; Fig. 1A) and exhibited symptoms typical for Wolfram syndrome (table S1). Although WFS1 protein abundance was decreased in all patients (Fig. 1B), *WFS1* mRNA expression was only decreased in patients 3 and 4 (Fig. 1C). These results suggested that different mutations resulted in distinct effects on mRNA expression and that *WFS1* loss-of-function mutations affected the production or stability of the protein. This conclusion is consistent with previous results, showing a decrease in the stability of mutant WFS1 protein overexpressed in COS-7 cells (*12*, *13*). Measurement of the mitochondrial membrane potential ($\Delta\psi_m$) using tetramethylrhodamine methyl ester (TMRM) dye after application of the mitochondrial uncoupler carbonyl cyanide *p*-trifluoromethoxyphenylhydrazone (FCCP) revealed similar $\Delta\psi_m$ in control and patient cells (Fig. 1D). We validated this result using the ratiometric JC-1 (5,5,6,6-tetrachloro-1,1,3,3-tetraethylbenzimidazolylcarbocyanine iodide) probe (Fig. 1, E and F), which confirmed that loss of function of WFS1 did not change $\Delta\psi_m$. Ultrastructural examination of mitochondria with transmission

[1]Institute of Neurosciences of Montpellier, INSERM, University of Montpellier, 34090 Montpellier, France. [2]PhyMedExp, University of Montpellier, INSERM, CNRS, CHRU Montpellier, 34295 Montpellier, France. [3]Department of Morphology, Surgery and Experimental Medicine, Section of Pathology, Oncology and Experimental Biology and Laboratory for Technologies of Advanced Therapies (LTTA), University of Ferrara, 44121 Ferrara, Italy. [4]Maria Cecilia Hospital, GVM Care & Research, Cotignola, 48033 Ravenna, Italy. [5]INSERM U1060, UMR INRA 1397, CarMeN Laboratory, Lyon 1 University, F-69003 Lyon, France. [6]Department of Ophthalmology, Angers University Hospital, 43933 Angers, France. [7]Singapore Eye Research Institute, Duke-NUS Graduate Medical School, 169857 Singapore, Singapore. [8]CHRU Montpellier, Centre of Reference for Genetic Sensory Diseases, CHU, Gui de Chauliac Hospital, 34090 Montpellier, France. [9]Laboratoire de Biologie Cellulaire, Université de Liège, Bât. B36 (Tour 4) GIGA—Neurosciences, Quartier Hôpital, Avenue Hippocrate 15, 4000 Liège 1, Belgium. [10]MMDN, Univ. Montpellier, EPHE, INSERM U1198, F-34095 Montpellier, France.
*These authors contributed equally to this work.
†Deceased.
‡These authors contributed equally to this work.
§Corresponding author. Email: cecile.delettre@inserm.fr (C.D.); benjamin.delprat@inserm.fr (B.D.)

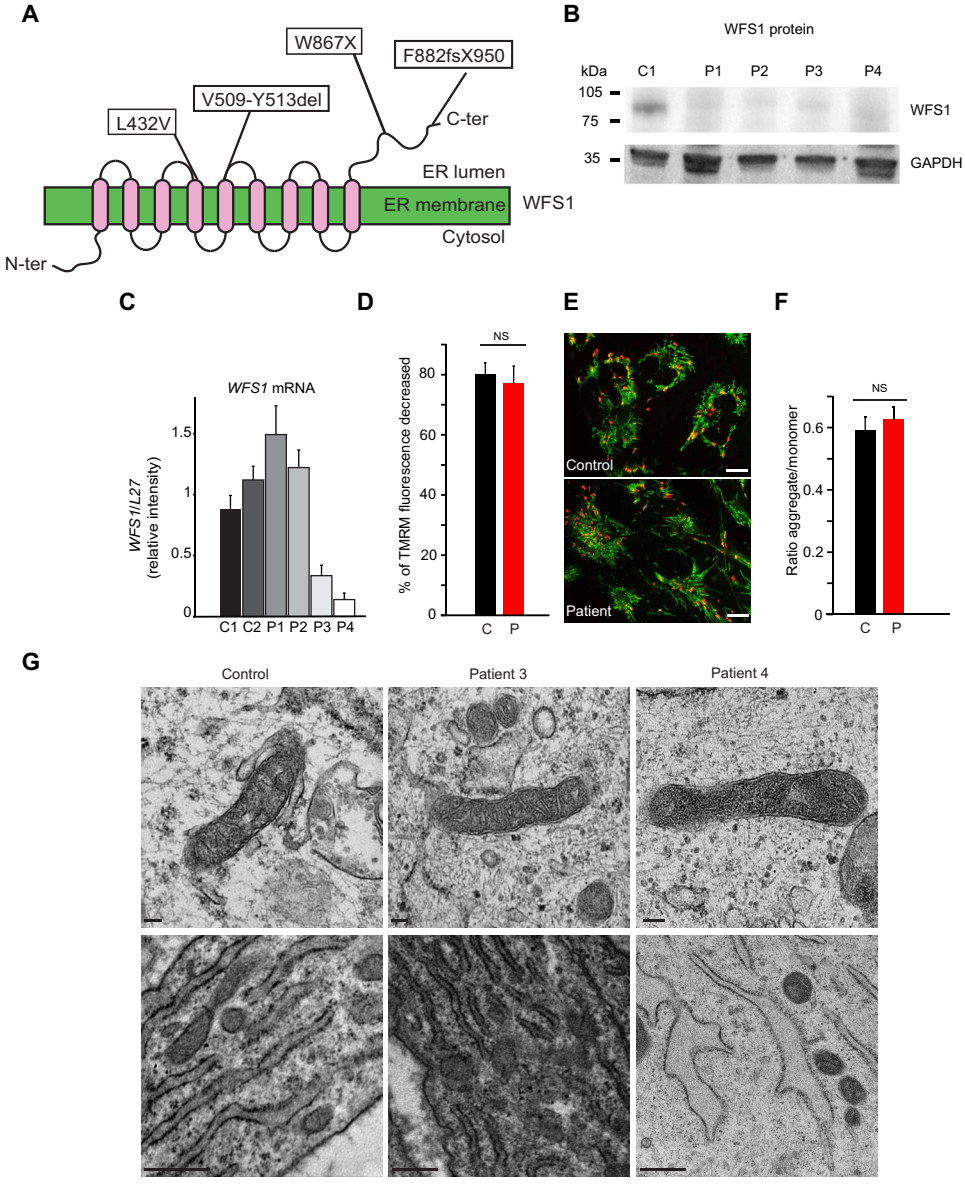

Fig. 1. WFS1-deficient fibroblasts have normal mitochondria. (**A**) Schematic representation of WFS1 showing the positions of the disease-causing mutations. (**B**) Immunoblot of lysates from control (C1) and patient fibroblasts (P1 to P4) for WFS1. Glyceraldehyde-3-phosphate dehydrogenase (GAPDH) was used as a loading control (n = 5 independent experiments). (**C**) Transcript levels of *WFS1* were quantified by reverse transcription quantitative polymerase chain reaction (RT-qPCR) in control (C1 and C2) and patient fibroblasts (P1 to P4). The mRNA levels were normalized to the reference gene *L27*. Error bars represent SEM. Controls, n = 9; P1, n = 6; P2, n = 6; P3, n = 6; P4, n = 5 independent experiments. (**D**) Assessment of $\Delta\psi_m$ with TMRM in control (C) (n = 36) and patient (P) (n = 34; P1, n = 10; P2, n = 7; P3, n = 9; P4, n = 8) fibroblasts. TMRM fluorescence was recorded continuously for 5 min before and after FCCP (1 μM) application. To enable comparison between groups, we calculated the percentage of TMRM fluorescence decreased by FCCP for each group. All data represent means ± SEM. NS, not significant. (**E**) $\Delta\psi_m$ in control (C) and patient (P) fibroblasts detected by the dye JC-1. Red fluorescence indicates the mitochondrial, aggregated form of JC-1. Green fluorescence indicates the monomeric form of JC-1. Scale bars, 10 μm. (**F**) Ratio of red to green fluorescence intensity, indicating the ratio of the aggregate to monomeric form of JC-1, in control (n = 24) and patient (n = 28) fibroblasts. Data are means ± SEM. (**G**) Ultrastructure of the mitochondria (top) and the ER (bottom) by TEM. Scale bars, 100 nm (top) and 500 nm (bottom).

electron microscopy (TEM) indicated that the overall structure (presence of a double membrane and presence of mitochondrial cristae located perpendicular to their major axis) and their form (elongated) were similar in patient and control cells (Fig. 1G). The exception was patient 4, whose cells had expanded ER (Fig. 1G). This ER morphology (dilated and irregular lumen) has been previously noted in *Wfs1*- or *Cisd2*-deficient cells (*14*, *15*).

WFS1 deficiency is associated with decreased mitochondrial Ca^{2+} uptake

WFS1 has been suggested to play a role in Ca^{2+} homeostasis by activating an inositol 1,4,5-trisphosphate receptor (IP_3R)–mediated Ca^{2+} release pathway (*16*), inhibiting sarco/endoplasmic reticulum Ca^{2+}-ATPase (SERCA) turnover and modifying the filling state of the ER Ca^{2+} store (*17*, *18*). WFS1 deficiency has also been suggested to lead to IP_3R dysfunction, disturbed cytosolic Ca^{2+} homeostasis, and altered mitochondrial dynamics (*11*). Accordingly, we hypothesized that the loss of function of the ER protein WFS1 affected Ca^{2+} flux between the ER-mitochondria through regulation of IP_3R. Coimmunoprecipitation experiments demonstrated that mouse WFS1 interacted with IP_3R (fig. S1). We then measured the effect of WFS1 loss of function on Ca^{2+} flux using the ER-targeted aequorin (erAEQ; Fig. 2A) (*19*). There were no significant differences in steady-state ER Ca^{2+} ($[Ca^{2+}]_{ER}$) between control and WFS1 patient fibroblasts (Fig. 2B). Next, we investigated the ER response to the Ca^{2+}-mobilizing agonist bradykinin, which activates G_q-coupled plasma membrane receptors to trigger the production of IP_3 and release of Ca^{2+} from the ER through the IP_3R. Before bradykinin stimulation, fibroblasts were transduced with the Ca^{2+}-sensitive FRET (fluorescence resonance energy transfer)–based cameleon protein D1-ER (Fig. 2C) (*20*). We found that mutated fibroblasts released 32% less ER Ca^{2+} than did control fibroblasts (Fig. 2D), suggesting that Wolfram syndrome patient fibroblasts release less Ca^{2+} through the IP_3R. To clarify whether loss of function of WFS1-suppressed IP_3-mediated cytosolic $[Ca^{2+}]$ signals was upstream or at the level of the IP_3Rs, we performed aequorin experiments in permeabilized cells stimulated with IP_3. In response to IP_3, patient fibroblasts released less Ca^{2+} from the ER than did control fibroblasts (Fig. 2, E and F). These results suggest that WFS1 loss impairs Ca^{2+} signaling directly at the level of IP_3R.

Depletion of ER Ca^{2+} with thapsigargin, a specific inhibitor of the SERCA pump, did not reveal differences in ER Ca^{2+} content between

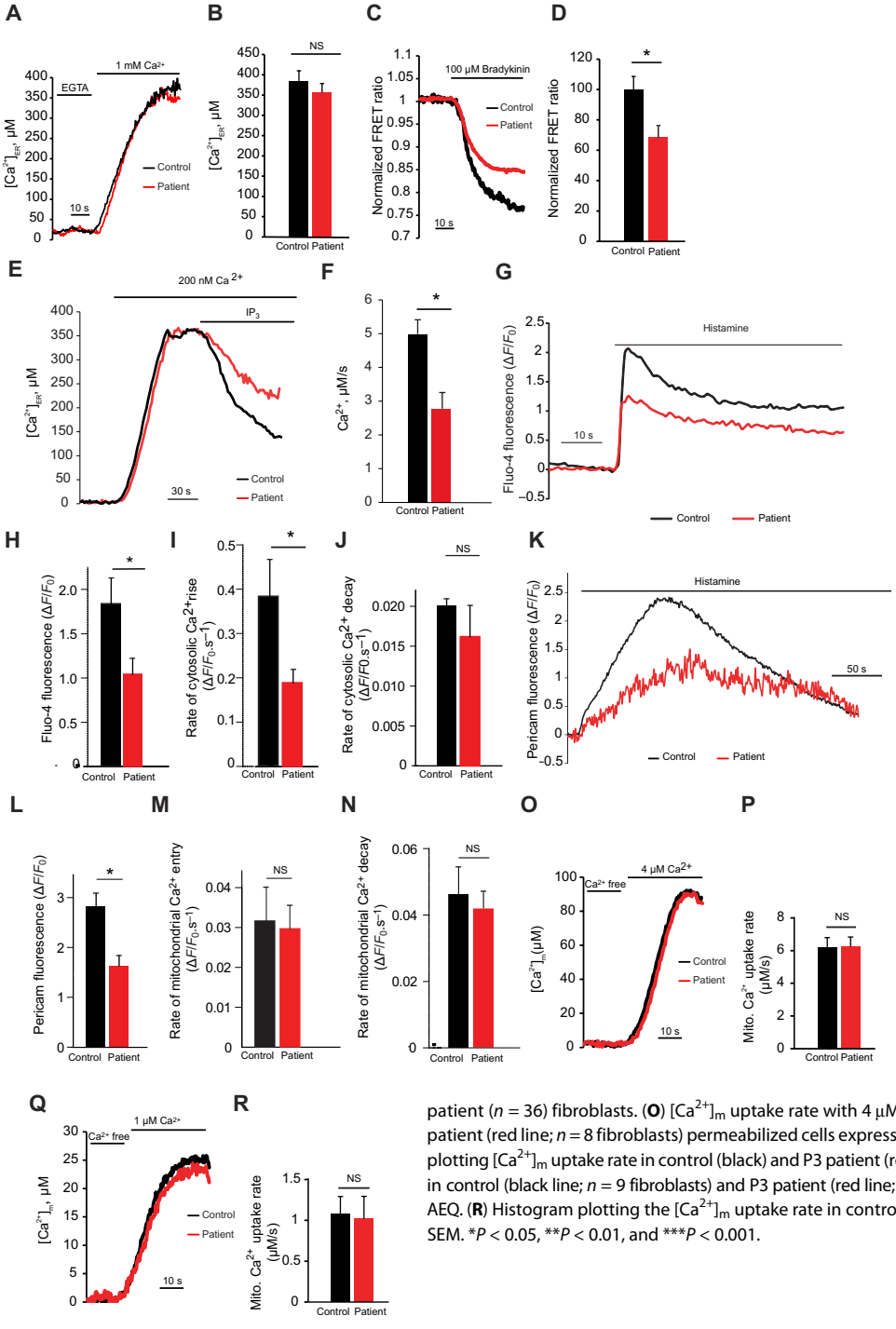

Fig. 2. Loss of function in WFS1 impairs Ca^{2+} homeostasis. (**A**) ER Ca^{2+} concentration ($[Ca^{2+}]_{ER}$) in control (black line; $n = 19$ fibroblasts) and P3 patient (red line; $n = 19$ fibroblasts) fibroblasts transiently expressing erAEQmut. (**B**) Histogram plotting $[Ca^{2+}]_{ER}$ steady-state level in control (black) and P3 patient (red) fibroblasts. (**C**) ER Ca^{2+} release induced by bradykinin (100 μM) in control (black; $n = 17$) and P3 patient (red; $n = 16$) fibroblasts transduced with the Ca^{2+}-sensitive FRET-based cameleon protein D1-ER. (**D**) Histogram plotting ER Ca^{2+} release in control (black) and P3 patient (red) cells. Data are means ± SEM. *$P < 0.05$. (**E**) ER Ca^{2+} concentration ($[Ca^{2+}]_{ER}$) in control (black line) and P3 patient (red line) fibroblasts transiently expressing erAEQ. After depletion of intracellular Ca^{2+} stores and aequorin reconstitution, cells were perfused in immunoblotting buffer. $CaCl_2$ was added to give a calculated free $[Ca^{2+}]$ of 500 nM. After steady state was achieved, IP_3 (5 M) was introduced to evoke ER-Ca^{2+} release. (**F**) Histogram plotting mean rates of Ca^{2+} release for the first 50 s after stimulation in control ($n = 12$) and patient ($n = 13$) fibroblasts. Data are presented as means ± SEM. *$P < 0.05$. (**G**) Representative cytosolic Ca^{2+} measured by Fluo-4 fluorescence in control (black line) and patient (red line) fibroblasts under histamine stimulation. (**H**) Maximum amplitude of Fluo-4 fluorescence in control ($n = 26$) and patient ($n = 35$) fibroblasts. (**I**) Rate of cytosolic Ca^{2+} rise in control ($n = 25$) and patient ($n = 35$) fibroblasts. (**J**) Rate of cytosolic Ca^{2+} decay in control ($n = 25$) and patient ($n = 35$) fibroblasts. (**K**) Representative mitochondrial Ca^{2+} ($[Ca^{2+}]_m$) as measured by pericam-mt fluorescence in control (black line) and patient (red line) fibroblasts stimulated with histamine. (**L**) Maximum amplitude of pericam-mt fluorescence in control ($n = 23$) and patient ($n = 36$) fibroblasts. (**M**) Rate of $[Ca^{2+}]_m$ entry in control ($n = 23$) and patient ($n = 36$) fibroblasts. (**N**) Rate of $[Ca^{2+}]_m$ decay in control ($n = 23$) and patient ($n = 36$) fibroblasts. (**O**) $[Ca^{2+}]_m$ uptake rate with 4 μM Ca^{2+} in control (black line; $n = 8$ fibroblasts) and P3 patient (red line; $n = 8$ fibroblasts) permeabilized cells expressing mitochondrial aequorin (mt-AEQ). (**P**) Histogram plotting $[Ca^{2+}]_m$ uptake rate in control (black) and P3 patient (red) fibroblasts. (**Q**) $[Ca^{2+}]_m$ uptake rate with 1 μM Ca^{2+} in control (black line; $n = 9$ fibroblasts) and P3 patient (red line; $n = 15$ fibroblasts) permeabilized cells expressing mt-AEQ. (**R**) Histogram plotting the $[Ca^{2+}]_m$ uptake rate in control (black) and P3 patient (red) cells. Data are means ± SEM. *$P < 0.05$, **$P < 0.01$, and ***$P < 0.001$.

controls and patients (fig. S2, A to D). Histamine induces IP_3R-dependent ER Ca^{2+} release from ER stores (*21*). As demonstrated by confocal imaging of cytoplasmic and mitochondrial $[Ca^{2+}]$ with Fluo-4 and the genetically encoded reporter pericam-mt, respectively, histamine-induced ER Ca^{2+} release in patient cells was decreased relative to that in control cells (Fig. 2G). In addition to the maximum peak amplitude, the rate of cytosolic Ca^{2+} rise (but not the rate of cytosolic Ca^{2+} decay) was also decreased in patient cells compared to control cells (Fig. 2, H to J). Ca^{2+} uptake by mitochondria was reduced in patient fibroblasts (Fig. 2, K and L). The rates of $[Ca^{2+}]_m$ entry and of $[Ca^{2+}]_m$ decay were similar in patient and control cells (Fig. 2, M and N). Because $\Delta\psi_m$ was not affected, the lack of $[Ca^{2+}]_m$ uptake in patient cells was not due to reduced driving force. To confirm these results, we performed experiments in digitonin-permeabilized cells perfused with medium at fixed $[Ca^{2+}]$. When Ca^{2+} was added back to the perfusion medium, the rates and peaks of $[Ca^{2+}]_m$ uptake were similar between control and patient cells (Fig. 2, O to R). Overall, these data suggest that the decrease in $[Ca^{2+}]_m$ uptake

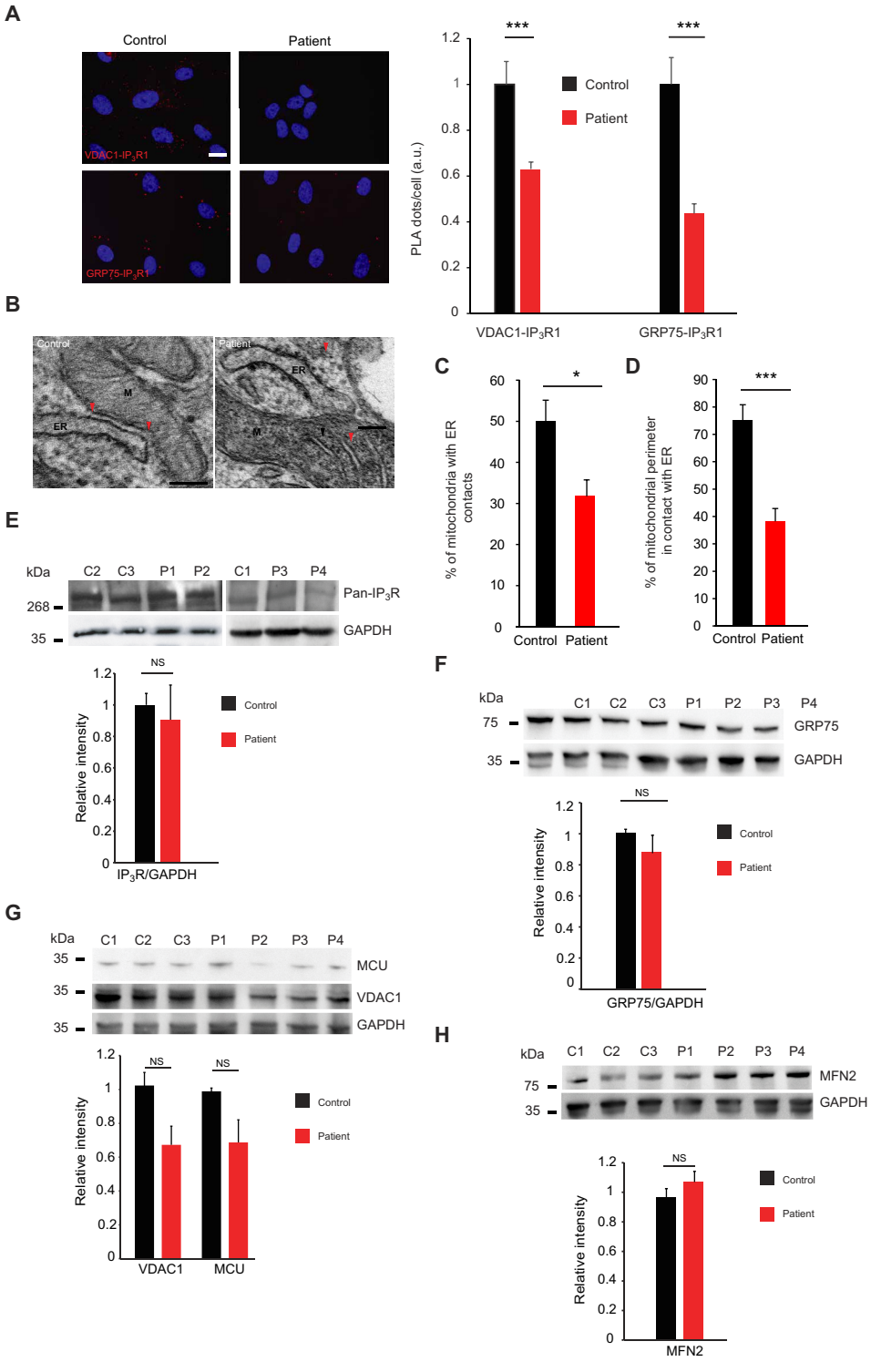

Fig. 3. Loss of function in WFS1 disruption MAM structure. (**A**) Representative PLA images (left) and quantitative analysis (right) of VDAC1-IP_3R1 and GRP75-IP_3R1 interactions in control and patient fibroblasts (8 to 21 images/controls and patients, $n = 56$ images for VDAC1-IP_3R1 and $n = 22$ to 43 images for GRP75-IP_3R1). a.u., arbitrary units. ***$P < 0.001$ compared to controls. Scale bar, 10 μm. (**B**) TEM of control and patient fibroblasts. The red arrowheads indicate the perimeter of mitochondria (M) in contact with ER. Scale bars, 100 nm. (**C**) Quantitative analysis of ER-mitochondria contacts in control and patient fibroblasts. Bar graph shows the percentage of mitochondria in contact with ER (means ± SEM, $n = 403$ mitochondria in control cells and $n = 659$ mitochondria in patient cells). *$P < 0.05$ compared to controls. (**D**) Quantification of mitochondrial length adjacent to ER normalized by total mitochondrial perimeter in control and patient fibroblasts. Bar graph shows the percentage of mitochondrial perimeter in contact with ER (means ± SEM, $n = 403$ mitochondria in control cells and $n = 659$ mitochondria in patient cells). ***$P < 0.001$ compared to controls. (**E**) Western blot (top) and densitometric analysis (bottom) of IP_3R protein abundance in control (C1 to C3, $n = 4$ experiments) and patient (P1, $n = 3$; P2, $n = 3$; P3, $n = 4$; P4, $n = 4$ experiments) fibroblasts. (**F**) Western blot (top) and densitometric analysis (bottom) of GRP75 protein abundance in control (C1 to C3, $n = 5$ experiments) and patient (P1, $n = 5$; P2, $n = 5$; P3, $n = 5$; P4, $n = 5$ experiments) fibroblasts. (**G**) Western blot (top) and densitometric analysis (bottom) of VDAC1 and MCU protein abundance in control (C1 to C3, $n = 3$ to 6 experiments) and patient (P1, $n = 4$; P2, $n = 4$; P3, $n = 6$; P4, $n = 6$ experiments) fibroblasts. (**H**) Western blot (top) and densitometric analysis (bottom) of MFN2 protein abundance in control (C1 to C3, $n = 4$ to 9 experiments) and patient (P1, $n = 5$; P2, $n = 6$; P3, $n = 4$; P4, $n = 4$ experiments) fibroblasts. GAPDH was used as a loading control (means ± SEM). n in (E) to (H) represents experiments.

of patient fibroblasts was due to decreased ER calcium release through IP_3R.

WFS1 deficiency is associated with decreased ER-mitochondria interactions

Cross-talk between ER and mitochondria is essential for processes in eukaryotic cells such as lipid synthesis and transport (*22*), mitochondrial functions (*23*), regulation of Ca^{2+} homeostasis (*24*), autophagy (*3*), and apoptosis (*25*). The ER directly communicates with mitochondria through close contacts referred to as MAMs, which are microdomains that enable efficient Ca^{2+} transfer between the ER and mitochondria. Ca^{2+} transfer from the ER into the mitochondria is facilitated by proteins that tether the two organelles together. IP_3R on the ER interacts with VDAC1 on the outer mitochondrial membrane through the molecular chaperone glucose-regulated protein 75 (GRP75) (*26*). The IP_3R/GRP75/VDAC1 complex also involves the $[Ca^{2+}]_m$ uniporter (MCU) on the inner mitochondrial membrane (*26*) to allow Ca^{2+} transfer from the ER to the mitochondrial matrix. To study the role of MAMs in Wolfram syndrome, we used in situ

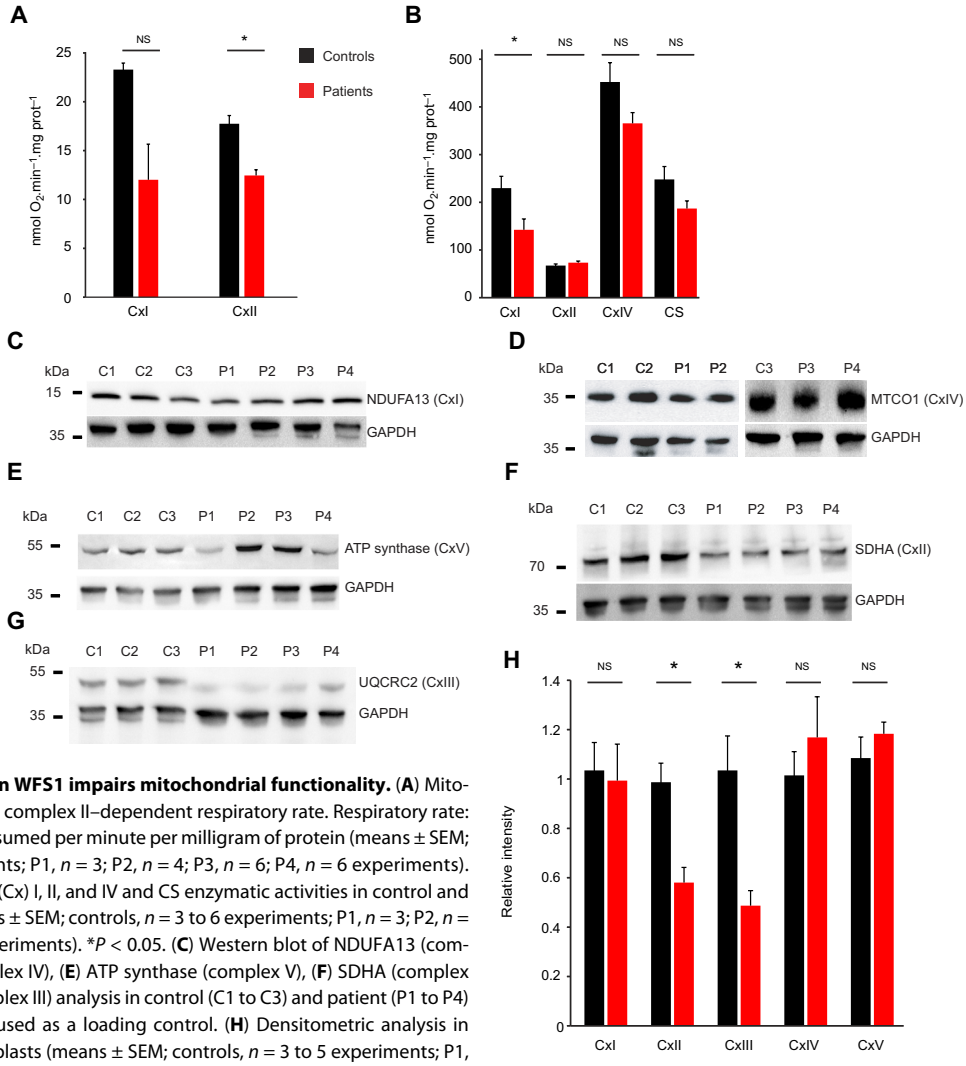

Fig. 4. Loss of function in WFS1 impairs mitochondrial functionality. (**A**) Mitochondrial complex I– and complex II–dependent respiratory rate. Respiratory rate: nanomole of oxygen consumed per minute per milligram of protein (means ± SEM; controls, $n = 5$ experiments; P1, $n = 3$; P2, $n = 4$; P3, $n = 6$; P4, $n = 6$ experiments). *$P < 0.05$. (**B**) Complexes (Cx) I, II, and IV and CS enzymatic activities in control and patient fibroblasts (means ± SEM; controls, $n = 3$ to 6 experiments; P1, $n = 3$; P2, $n = 3$; P3, $n = 5$; P4, $n = 5$ experiments). *$P < 0.05$. (**C**) Western blot of NDUFA13 (complex I), (**D**) MTCO1 (complex IV), (**E**) ATP synthase (complex V), (**F**) SDHA (complex II), and (**G**) UQCRC2 (complex III) analysis in control (C1 to C3) and patient (P1 to P4) fibroblasts. GAPDH was used as a loading control. (**H**) Densitometric analysis in control and patient fibroblasts (means ± SEM; controls, $n = 3$ to 5 experiments; P1, $n = 5$; P2, $n = 5$; P3, $n = 7$; P4, $n = 7$ experiments). *$P < 0.05$ compared to control.

proximity ligation assay (PLA) to detect and quantify both VDAC1-IP_3R1 and GRP75-IP_3R1 interactions at the MAM interface in fixed fibroblasts, as previously described (*27*). We found significantly reduced VDAC1-IP_3R1 and GRP75-IP_3R1 interactions in patient fibroblasts compared to control fibroblasts (−70% and −56%, respectively), indicating reduced ER-mitochondria interactions in patient fibroblasts (Fig. 3A). To confirm this observation, we evaluated the percentage of mitochondria in close contact with ER in control and patient cells with TEM morphometric analysis (Fig. 3, B to D, and table S2). Mitochondria-ER associations were found in control and patient cells (Fig. 3B). However, the percentage of mitochondria with ER contact was significantly reduced by 49% in patient cells (Fig. 3C). To evaluate more precisely the importance of these contacts, we measured the percentage of mitochondria perimeter in contact with the ER, and this value was significantly reduced by 38% in patient cells (Fig. 3D). However, there were no significant differences in the protein abundance of IP_3R (Fig. 3E), GRP75 (Fig. 3F), VDAC1, MCU (Fig. 3G), or MFN2 (Fig. 3H), another protein that regulates the tethering of the ER to mitochondria (*28*).

WFS1 deficiency impairs mitochondrial functionality

Reduced $[Ca^{2+}]_m$ uptake might adversely affect various metabolic pathways, resulting in altered energy production. We evaluated mitochondrial functionality by analyzing oxygen consumption and the enzymatic activity of complexes and citrate synthase (CS). WFS1 patient cells exhibited a significant decrease (30%) in complex II–driven respiration (Fig. 4A), and complex I–driven respiration was decreased in cells from three of four patients (fig. S3). To understand the cause of the decreased mitochondrial respiration in patient fibroblasts, we assessed the activities of respiratory chain complexes I [NADH (reduced form of nicotinamide adenine dinucleotide) ubiquinone reductase], II (succinate ubiquinone reductase), and IV (cytochrome c oxidase) in cell homogenates. The activity of complex I was significantly decreased in patient cells (40%), whereas the activity of complexes II and IV were similar between patient and control cells (Fig. 4B). No changes were observed in CS activity (Fig. 4B), suggesting that mitochondrial mass was normal. Therefore, we measured the protein abundance of selected subunits of each complex in the mitochondrial electron transport chain. The protein

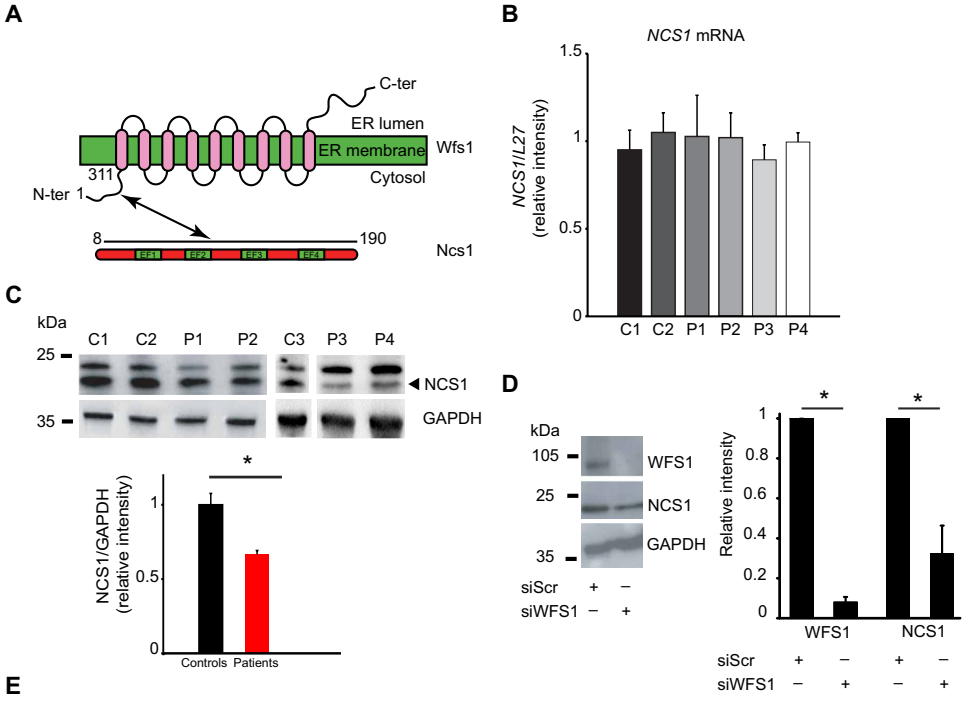

Fig. 5. WFS1 interacts with NCS1 and modulates its abundance. (**A**) Schematic representation of the interaction site between mouse Wfs1 and Ncs1 identified by yeast two-hybrid screening. A fragment encompassing amino acids 1 to 311 of human WFS1 was used for the yeast two-hybrid screening. EF-hand motifs in Ncs1 are helix-loop-helix structural domains found in a large family of Ca^{2+} binding proteins. (**B**) Transcript levels of *NCS1* were quantified by RT-qPCR in control (C1 and C2) and patient fibroblasts (P1 to P4). The mRNA levels were normalized to the reference gene *L27* (means ± SEM; controls, $n = 9$; P1, $n = 6$; P2, $n = 6$; P3, $n = 6$; P4, $n = 5$ independent experiments). (**C**) Immunoblot of lysates from control (C1 to C3) and patient fibroblasts (P1 to P4) for NCS1. GAPDH was used as a loading control. The immunoblot bands were quantified by densitometry, and the NCS1/GAPDH ratios were calculated (controls, $n = 4$; P1, $n = 4$; P2, $n = 4$; P3, $n = 5$; P4, $n = 5$ independent experiments). (**D**) Western blot analysis and quantification of control fibroblasts transfected with scrambled siRNA (siScr) or WFS1 siRNA (siWFS1). WFS1 and NCS1 protein abundance were analyzed 72 hours after siRNA transfection. Data are means ± SEM from $n = 7$ independent experiments. *$P < 0.05$. (**E**) Subcellular fractions prepared from mouse brain tissue were immunoblotted for HSP60 (a mitochondrial marker), SIL1 (an ER marker), VDAC1 (a MAM marker), and NCS1. H, homogenate; ER, endoplasmic reticulum fraction; Mp, pure mitochondrial fraction; MAMs, mitochondria-associated membrane fraction.

abundance of complex I (NDUFA13; Fig. 4C), complex IV (MTCO1; Fig. 4D), and complex V [adenosine 5′-triphosphate (ATP) synthase; Fig. 4E] subunits did not differ between control and patient cells. Patient cells showed a decrease in the protein abundance of complex II (SDHA; Fig. 4F) and complex III (UQCRC2) subunits (Fig. 4G). Protein abundance was quantified for each complex (Fig. 4H).

WFS1 regulates mitochondrial functionality through NCS1

We sought to identify protein partners of the cytosolic domain of WFS1 by performing a yeast two-hybrid analysis using residues 1 to 311 of murine Wfs1 as bait to screen a random-primed complementary DNA (cDNA) library prepared from mouse inner ear. A total of 29 positive colonies were obtained (table S3). We identified mouse Ncs1 as an interacting partner (Fig. 5A). NCS1 is an EF-hand cytosolic protein preferentially expressed in neurons (*29*) that regulates IP_3R (*30*–*32*) and the dopamine D2 receptor (*33*). We confirmed the interaction of NCS1 with Myc-tagged WFS1 and with endogenous IP_3R by coimmunoprecipitation (fig. S4, A and B). Although fibroblast *NCS1* mRNA expression levels were similar between control and patient fibroblasts (Fig. 5B), NCS1 protein levels were decreased by almost 50% in patient fibroblasts (Fig. 5C). Consistent with this observation, knockdown of WFS1 using short interfering RNA (siRNA) in control fibroblasts decreased NCS1 protein levels by 60% (Fig. 5D and fig. S5). Together, these results suggest that WFS1 regulates NCS1 protein stability, which is consistent with the ability of WFS1 to regulate the stability of other proteins, such as HRD1 (*34*) and SERCA (*18*), through the ubiquitin proteasome pathway. Last, because IP_3R and WFS1 are localized in MAMs (*35*–*37*), we looked at the cellular distribution of NCS1 in mouse brain subjected to subcellular fractionation. NCS1 was not only localized mainly in the ER and in MAMs (Fig. 5E) but also faintly detected in the mitochondrial fraction (Fig. 5E), which might be due to its interaction with PINK1 (*38*).

Knockdown of NCS1 impairs Ca^{2+} homeostasis and mitochondrial function

To elucidate the role of NCS1 in mitochondrial function, we used siRNAs to deplete NCS1 in human fibroblasts (fig. S6). Similar to Wolfram syndrome patient cells, histamine-mediated Ca^{2+} release was reduced in cells with NCS1 knockdown (Fig. 6A), specifically the maximum peak amplitude and the rate of cytosolic Ca^{2+} rise (Fig. 6, B and C) but not the rate of cytosolic Ca^{2+} decay (Fig. 6D). In addition, $[Ca^{2+}]_m$ uptake was significantly reduced in NCS1-deficient cells (Fig. 6E). Although the maximum peak amplitude was reduced in cells with NCS1 knockdown (Fig. 6F), $[Ca^{2+}]_m$ entry and decay were similar between siNCS1- and siScr-treated cells (Fig. 6, G and H). Knockdown of NCS1 led to a decrease in both complex I– and complex II–driven respiration, similar to that observed in patient fibroblasts (Fig. 6I). Moreover, NCS1 knockdown also decreased VDAC1 and SDHA (complex II) protein abundance compared to controls (Fig. 6J) and the proportion of mitochondria contacting ER (Fig. 6K). These results demonstrated that NCS1 modulated $[Ca^{2+}]_m$ uptake and could be a key determinant to maintain mitochondrial function and MAM integrity.

Reexpression of NCS1 rescues the defective mitochondrial phenotype of WFS1-deficient cells

Given the effect of NCS1 on ER-$[Ca^{2+}]_m$ uptake and respiratory chain function and to validate our hypothesis, we investigated

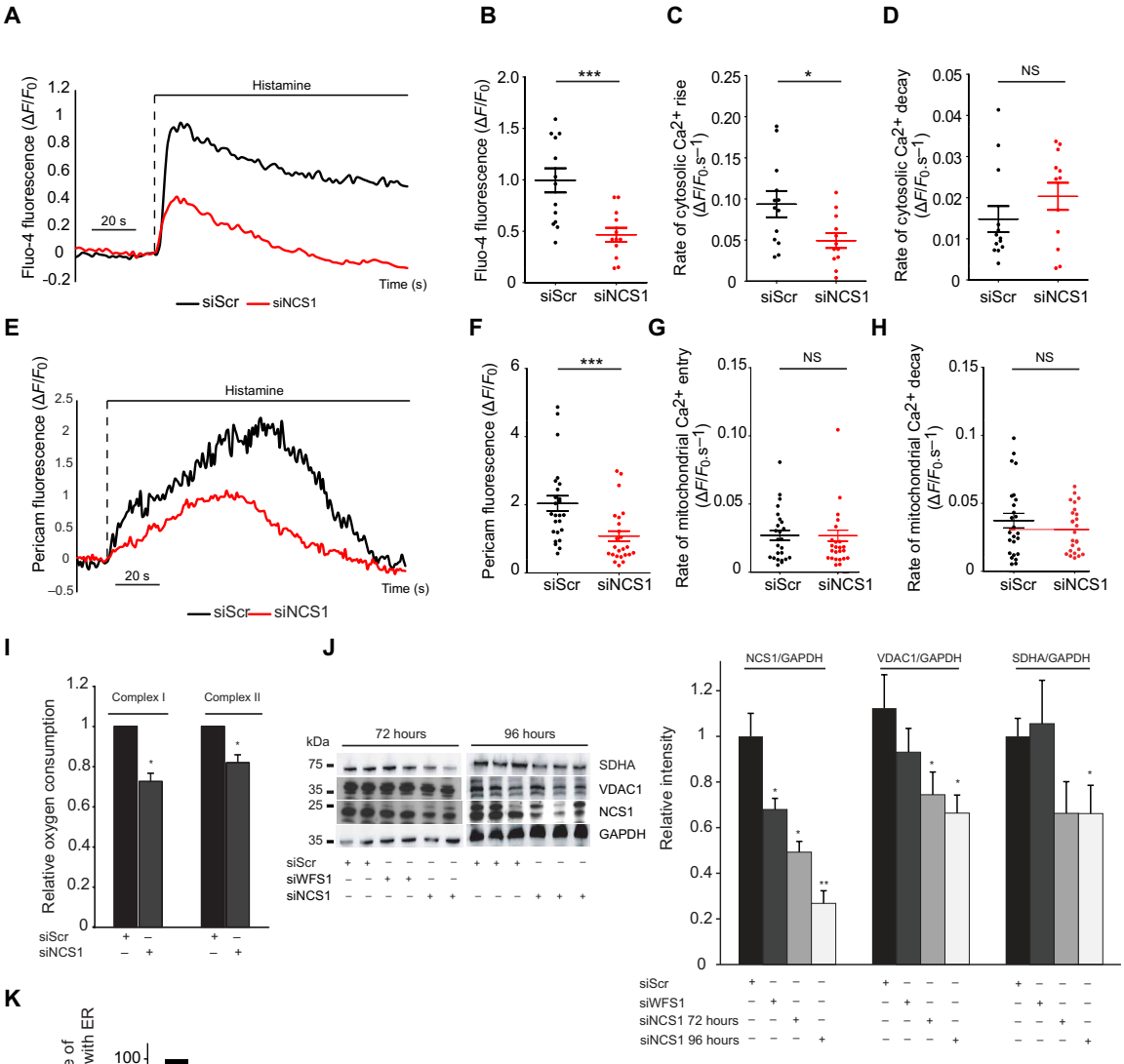

Fig. 6. NCS1 knockdown impairs Ca^{2+} homeostasis and mitochondrial function. (**A**) Representative cytosolic Ca^{2+} measured by Fluo-4 fluorescence in control fibroblasts treated with nontargeting siScr (black line) or siNCS1 (red line) and stimulated with histamine. (**B**) Maximum amplitude of Fluo-4 fluorescence in control fibroblasts treated with nontargeting siScr (black line; $n = 13$ cells) or siNCS1 (red line; $n = 12$ cells). (**C**) Rate of cytosolic Ca^{2+} rise in control fibroblasts treated with nontargeting siScr (black line; $n = 13$ cells) or siNCS1 (red line; $n = 12$ cells). (**D**) Rate of cytosolic Ca^{2+} decay in control fibroblasts treated with nontargeting siScr (black line; $n = 13$ cells) or siNCS1 (red line; $n = 12$ cells). (**E**) Representative $[Ca^{2+}]_m$ measured by pericam-mt fluorescence in control fibroblasts treated with nontargeting siScr (black line) or siNCS1 (red line). (**F**) Maximum amplitude of pericam-mt fluorescence in control fibroblasts treated with nontargeting siScr (black dots; $n = 25$ cells) or siNCS1 (red dots; $n = 24$ cells). (**G**) Rate of $[Ca^{2+}]_m$ entry in control fibroblasts treated with nontargeting siScr (black line; $n = 25$ cells) or siNCS1 (red line; $n = 24$ cells). (**H**) Rate of $[Ca^{2+}]_m$ decay in control fibroblasts treated with nontargeting siScr (black line; $n = 25$ cells) or siNCS1 (red line; $n = 24$ cells). (**I**) Complex I– and complex II–mediated respiration of control fibroblasts transfected with nontargeting siRNA (siScr) or NCS1 siRNA (siNCS1) (means ± SEM, $n = 3$ experiments). (**J**) Effect of NCS1 and WFS1 knockdown on NCS1, VDAC1, and SDHA (complex II) protein abundance in control fibroblasts transfected with nontargeting (siScr), NCS1 (siNCS1), or WFS1 (siWFS1) siRNA. NCS1 knockdown effect is shown 72 and 96 hours after siRNA transfection. GAPDH was used as a loading control. The immunoblot bands were quantified by densitometry, and the intensity of the NCS1, VDAC1, and SDHA bands was calculated (means ± SEM, $n = 7$ experiments). (**K**) Effect of NCS1 knockdown on ER-mitochondria contact. Bar graph shows the relative percentage of mitochondria in contact with ER ($n = 257$ mitochondria for siScr and $n = 239$ mitochondria for siNCS1). *$P < 0.05$, **$P < 0.01$, and ***$P < 0.001$.

whether overexpression of NCS1 in patient fibroblasts could rescue mitochondrial dysfunction. Transfection and subsequent expression of NCS1 in WFS1-deficient cells were confirmed by immunoblotting (Fig. 7A). Histamine-induced ER Ca^{2+} release was not statistically significant between patient cells overexpressing NCS1 and control cells (Fig. 7B and fig. S7A). NCS1 overexpression did not alter the rate of cytosolic Ca^{2+} rise but increased the rate of Ca^{2+} decay (Fig. 7, C and D). In addition, NCS1 overexpression in patient cells restored normal $[Ca^{2+}]_m$ uptake (Fig. 7E and fig. S7B) by correcting the rate of $[Ca^{2+}]_m$ entry and decay (Fig. 7, F and G). Moreover, NCS1

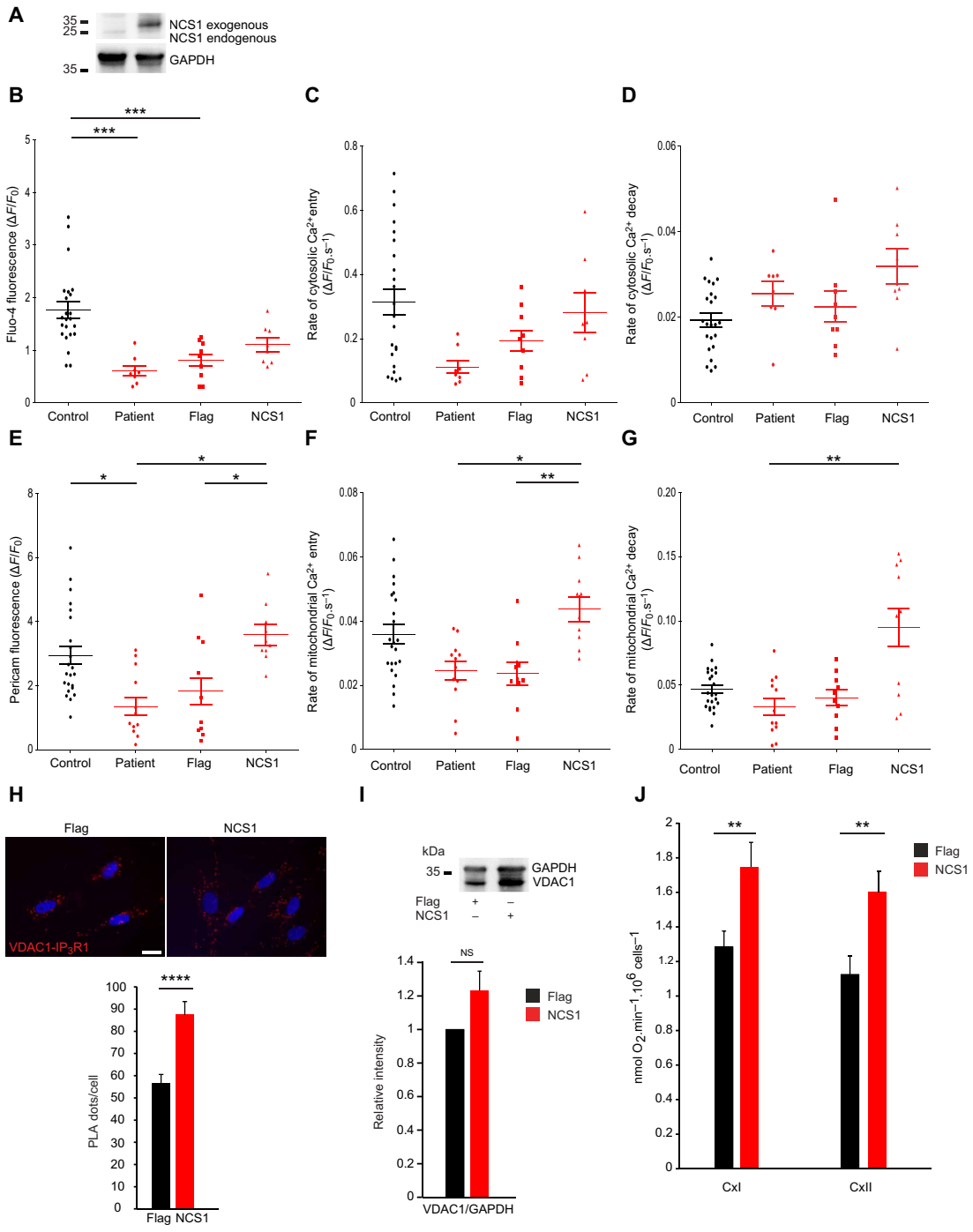

Fig. 7. NCS1 overexpression restores mitochondrial function. (**A**) Expression of NCS1 in patient fibroblasts transfected with Flag alone (Flag) or NCS1-Flag (NCS1). GAPDH was used as a loading control. (**B**) Maximum amplitude of histamine-stimulated Fluo-4 fluorescence in control fibroblasts (black dots; $n = 23$), P3 patient fibroblasts (red dots; $n = 8$), P3 patient fibroblasts expressing Flag alone (red squares; $n = 9$), and P3 patient fibroblasts expressing NCS1-Flag (red triangles; $n = 8$). (**C**) Rate of cytosolic Ca^{2+} rise in control fibroblasts (black dots), P3 patient fibroblasts (red dots), P3 patient fibroblasts expressing Flag alone (red squares), and P3 patient fibroblasts expressing NCS1-Flag (red triangles). Same n values as (B). (**D**) Rate of cytosolic Ca^{2+} decay in control fibroblasts (black dots), P3 patient fibroblasts (red dots), P3 patient fibroblasts expressing Flag alone (red squares), and P3 patient fibroblasts expressing NCS1-Flag (red triangles). Same n values as (B). (**E**) Maximum amplitude of histamine-stimulated pericam-mt fluorescence in control fibroblasts (black dots; $n = 23$), P3 patient fibroblasts (red dots; $n = 12$), P3 patient fibroblasts expressing Flag alone (red squares; $n = 10$), and P3 patient fibroblasts expressing NCS1-Flag (red triangles; $n = 10$). (**F**) Rate of $[Ca^{2+}]_m$ entry in control (black dots), P3 patient (red dots), P3 patient treated with Flag alone (red squares), and P3 patient treated with NCS1-Flag (red triangles). Same n values as (E). (**G**) Rate of $[Ca^{2+}]_m$ decay in control fibroblasts (black dots), P3 patient fibroblasts (red dots), P3 patient fibroblasts expressing Flag alone (red squares), and P3 patient fibroblasts expressing NCS1-Flag (red triangles). Same n values as (E). Means ± SEM; $n = 8$ to 28 cells. $^*P < 0.05$, $^{**}P < 0.01$, $^{***}P < 0.001$. (**H**) Representative PLA images (top) and quantitative analysis (bottom) of VDAC1-IP_3R1 interactions in patient fibroblasts transfected with Flag alone or NCS1-Flag (NCS1; $n = 94$ and 156, respectively). $^{****}P < 0.0001$ compared to controls. Scale bar, 10 μm. (**I**) Effect of NCS1 overexpression on VDAC1 protein expression in patient fibroblasts with Flag alone (Flag) or NCS1-Flag (NCS1). GAPDH was used as a loading control. The immunoblot bands were quantified by densitometry, and VDAC1 intensity was calculated (means ± SEM; $n = 6$ experiments). (**J**) Complex I– and complex II–mediated respiration of patient fibroblasts transfected with Flag alone (Flag) or NCS1-Flag (NCS1) (means ± SEM; $n = 4$ experiments). $^{**}P < 0.01$.

expression increased the number of VDAC1-IP_3R1 interactions in MAMs by 40% in patient cells compared to control cells (Fig. 7H). Although overexpression of NCS1 in patient cells did not significantly modify the protein abundance of VDAC1 (Fig. 7I) and that of other proteins of the respiratory chain complexes (fig. S8, A to F), mitochondrial respiration analysis showed that the NCS1 overexpression in WFS1-deficient cells was associated with a statistically significant increase in complex I– and complex II–driven respiration (Fig. 7J). These data indicate that NCS1 rescue could protect WFS1-deficient cells and could be used as a tool to restore mitochondrial function.

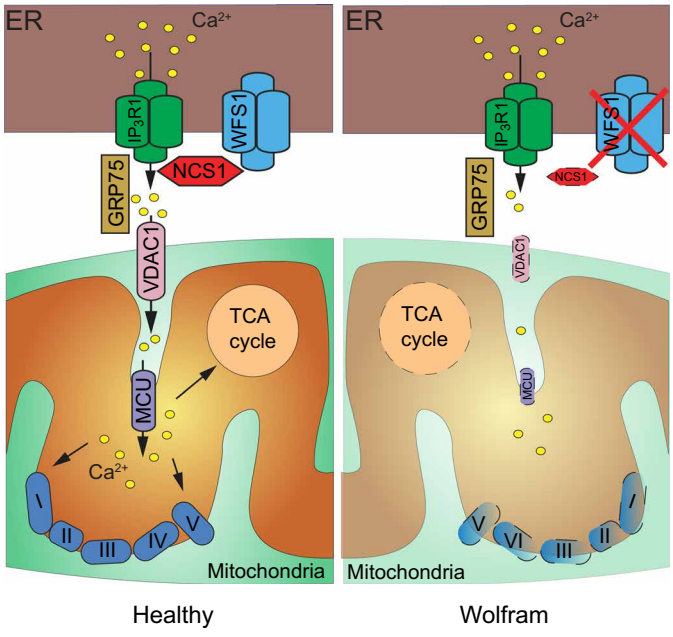

Fig. 8. Model of mitochondrial alteration induced by loss of function of WFS1. (**Left**) In healthy cells, WFS1 binds to NCS1 to form a complex with IP_3R1 to activate ER-mitochondria Ca^{2+} transfer to promote mitochondrial function. When the WFS1/NCS1/IP_3R1 complex and VDAC1 are functional, Ca^{2+} can properly transfer from the ER to mitochondria and activate the TCA cycle and mitochondrial respiratory chain. (**Right**) In Wolfram syndrome, the loss of function of WFS1 leads to NCS1 degradation and decreased ER-mitochondria Ca^{2+} transfer. As a consequence, the mitochondrial respiratory chain is altered.

DISCUSSION

Our study provides new insights into mechanisms underlying the mitochondrial dysfunction in WFS1-deficient cells involving NCS1, a WFS1 interacting protein. We demonstrated that WFS1 interacted with the Ca^{2+} sensor NCS1 (*39*) and that NCS1 protein abundance was substantially decreased in WFS1-deficient cells. Addition of NCS1 to planar lipid bilayers or overexpression of NCS1 in PC12 cells results in increased IP_3R channel activity (*30*–*32*), which should lead to increased Ca^{2+} release from the ER. In fibroblasts from our Wolfram syndrome patients, a decrease in Ca^{2+} flux from the ER was observed only under histamine application, whereas ER Ca^{2+} load was unchanged, suggesting a role of NCS1 in regulating IP_3R activity. In addition, there was a concomitant decrease in the $[Ca^{2+}]_m$ uptake. We further showed that ER-mitochondria structural interactions were reduced in patient cells, as evidenced by reduced interactions of two pairs of proteins at the MAM interface (VDAC1-IP_3R1 and GRP75-IP_3R1). This reduced tethering likely contributed to reduced Ca^{2+} transfer from ER to mitochondria in these patient cells, as has been previously described in MFN2-deficient cells that show a decrease in MAM tethering (*28*, *40*). Dysregulation of Ca^{2+} homeostasis and impaired MAM formation have been previously described in WFS2-deficient cells (*41*, *42*), suggesting a common pathophysiological mechanism. In many neurodegenerative diseases, the contact between ER and mitochondria is decreased (*43*), similar to what we observed in WFS1 patients. Specifically, in Alzheimer's disease, the number of contacts is increased (*44*), similar to what is observed in Wolfram syndrome patients. Moreover, in amyotrophic lateral sclerosis type 8 (ALS8), the number of ER-mitochondria contacts is increased, and in ALS16 (*45*), the number is decreased. These two observations are similar to what is observed in Wolfram syndrome. It seems that the number of ER-mitochondria contacts depends on the protein affected. MAM structure and function are tightly regulated to ensure proper functioning of the mitochondria. Any modification in the structure and/or function will lead to a dysfunction of mitochondrial respiration that will have repercussions on cellular physiology.

Although the reduction of $[Ca^{2+}]_m$ uptake was not attributed to a change in $\Delta\psi_m$, it may have resulted from two factors: the decrease in the ER Ca^{2+} release and disorganization of the MAMs. One limitation of the study was the small number of patients from whom fibroblasts were analyzed because of the extreme rarity of the pathology. Rescue experiments for WFS1 failed to express the protein; however, down-regulation or overexpression of NCS1 in cells confirms the results, reinforcing the robustness of analyses of patient cells and suggesting that NCS1 is involved in Ca^{2+} and MAM dysregulation in Wolfram syndrome. The reduced $[Ca^{2+}]_m$ uptake impairs the function of the mitochondria, because some dehydrogenases of the tricarboxylic acid (TCA) cycle require Ca^{2+} to maintain complex I and complex III and V function. There is no evidence that Ca^{2+} controls the abundance of complex II. Nakamura *et al.* (*46*) have found that the loss of NCS1 in mouse cardiomyocytes alters the proper functioning of the mitochondria by decreasing ATP levels and the respiratory rate, which is associated with a decrease in complex I, III, and V protein abundance. Consistent with this work, cells from our Wolfram syndrome patients showed a substantial decrease in mitochondrial respiratory chain activity. The decrease in complex II–driven respiration is probably linked to the decrease in complex II expression.

The clinical hallmark of Wolfram syndrome is the association of diabetes mellitus and optic atrophy, due respectively to degeneration of pancreatic β cells and retinal ganglion cells (*47*), two cell types in which NCS1 is abundant (*48*, *49*). In β cells, NCS1 localizes mainly in the cytosol, ER, and secretory granules. NCS1 promotes the priming of the secretory granules for release and increases the number of granules residing in the readily releasable pool. This action is mediated by an activation of the phosphatidylinositol 4-kinase β (*48*). In MIN6 pancreatic β cells, WFS1 knockdown reduces insulin secretion, which is associated with a decrease in cytosolic Ca^{2+} (*50*). It is tempting to speculate that this dysfunction could be due to the possible loss of NCS1. In retinal ganglion cells, NCS1 may be involved in synaptogenesis during development and in synaptic transmission upon maturation (*49*). These two processes depend on energy supplied by mitochondria transported along axons to the synaptic terminals (*51*, *52*) notably to maintain Ca^{2+} homeostasis (*53*, *54*). Efficient axonal transport of mitochondria depends on their own energy production, because axonal transport is ATP dependent and, on cytoskeletal-mitochondrial interaction, because axonal transport is microtubule based (*55*). Our data, combined with the work of Cagalinec *et al.* (*11*), suggest that altered Ca^{2+} homeostasis due to decreased NCS1 protein abundance may be responsible for the impaired mitochondrial dynamics. Our data provide a potential explanation for the defective transport of mitochondria along the retinal ganglion cell axons because when NCS1 is diminished, as would be expected in WFS1-deficient retinal ganglion cells, mitochondrial function is impaired. This defect may be responsible for the retinal ganglion cell degeneration observed in Wolfram syndrome patients.

Wolfram syndrome patients may develop psychiatric disorders (*56*), such as bipolar disorder, schizophrenia, anxiety, and depression

(*57*–*59*). Surprisingly, changes in NCS1 abundance provoke similar symptoms in human and mice (*60*, *61*). It is tempting to speculate that the neurological and psychiatric disorders are linked to destabilization of NCS1 expression levels. In line with this, Schlecker *et al.* (*31*) have demonstrated that lithium promotes the interaction of IP_3R and NCS1 and in bipolar disorder.

In this study, we demonstrated that WFS1, NCS1, and IP_3R may be part of a complex associated with ER-mitochondria contact sites. In healthy cells, WFS1 interacts with NCS1 and may prevent its degradation. Our studies of the interactions between IP_3R and NCS1 have used coimmunoprecipitation (*31*) or PLA (*30*), approaches that do not allow us to conclude whether the interaction is direct. It is possible that another protein interacts with either NCS1 or IP_3R to bridge the two proteins. Nevertheless, the modulation of IP_3R function by NCS1 favors a direct interaction. When the WFS1/NCS1/IP_3R complex is functional, Ca^{2+} can be properly transferred from the ER to mitochondria and activate the TCA cycle and the mitochondrial respiratory chain. When WFS1 is lost, the WFS1/NCS1/IP_3R complex is disrupted and NCS1 is partially degraded or destabilized. Consequently, altered ER-$[Ca^{2+}]_m$ transfer leads to mitochondrial bioenergetic dysfunction that may result in the activation of cell death in the tissues affected by Wolfram syndrome (Fig. 8). We show that NCS1 overexpression in Wolfram syndrome patient fibroblasts reverses most of the observed defects. As a consequence, NCS1 may be a drug target for the treatment of Wolfram syndrome.

MATERIALS AND METHODS

Cell cultures

Fibroblasts were cultured from skin biopsies taken after obtaining informed consent from three individuals without diabetes mellitus and four affected patients carrying mutations in *WFS1* gene, as previously described (*62*). Human embryonic kidney (HEK) 293T cells were cultured in MegaCell Dulbecco's Modified Eagle's Medium (Sigma-Aldrich, St. Louis, MO, USA) supplemented with 10% fetal bovine serum (Sigma-Aldrich) and 20 mM penicillin/streptomycin (Sigma-Aldrich).

Cell transfection

Control fibroblasts were transfected with siRNA directed against WFS1 (ON-TARGETplus Human WFS1 siRNA SMARTpool, Thermo Fisher Scientific Biosciences, Waltham, MA, USA) and/or with siRNA directed against NCS1 (ON-TARGETplus Human NCS1 siRNA SMARTpool, Thermo Fisher Scientific Biosciences) using Lipofectamine 2000 (Invitrogen, Carlsbad, USA) according to the manufacturer's instructions and processed 72 or 96 hours later for Western blot or oxygraphy analyses. Transfection with ON-TARGET Non-Targeting Pool (siScr) was used as controls.

To overexpress NCS1-Flag or pericam-mt vectors, fibroblasts were transfected by nucleofection. Nucleofection was performed according to an optimized protocol provided by the manufacturer (Amaxa Biosystems, Cologne, Germany). Cells were suspended in 100 µl of nucleofactor solution (Amaxa Biosystems); mixed with pericam-mt, Flag, or NCS1-Flag construct; and subjected to nucleofection, after which cells were transferred into prewarmed fresh medium. Cells were analyzed 24 hours after nucleofection.

Real-time RT-PCR

Real-time PCR was performed on total RNA extracted from cells using the RNeasy Mini Kit (Qiagen, Venlo, Netherlands) and reverse transcribed with the SuperScript III First-Strand Kit (Invitrogen) according to the manufacturer's instructions.

Measurements of enzymatic activity and protein content

The activity of the mitochondrial respiratory chain complexes and respiratory rates was measured on cell homogenates, as described previously (*62*). The activity of the mitochondrial respiratory chain complexes was measured with cell homogenates in a cell buffer [250 mM saccharose, 20 mM tris(hydroxymethyl)aminomethane, 2 mM EGTA, and bovine serum albumin (BSA; 1 mg/ml) (pH 7.2)] at 37°C using a UV-SAFAS spectrophotometer (SAFAS). Cellular protein content was determined with the BCA (bicinchoninic assay) Kit (Pierce) using BSA as a standard. Complex I (NADH ubiquinone reductase, EC 1.6.5.3) activity was measured according to a procedure described elsewhere (*63*) and adapted using 2,6-dichloroindophenol (DCPIP) to avoid the inhibition of complex I activity by decylubiquinol (*64*). Cells were disrupted by two freezing-thawing cycles, washed, centrifuged for 1 min at 16,000*g*, and resuspended in cell buffer (50 µl per 10^6 cells). Complex II (succinate ubiquinone reductase) activity was measured according to James and colleagues (*65*). Specific enzymatic activities of complexes I and II were expressed in mIU (nanomoles of DCPIP per minute per milligram of protein). Complex IV (cytochrome c oxidase) activity was recorded according to a method that Rustin and colleagues (*66*) adapted in a 50 mM KH_2PO_4 buffer, using 15 µM reduced cytochrome c. Specific enzymatic activity was expressed in mIU (nanomoles of cytochrome c per minute per milligram of protein). CS activity was assayed by a standard procedure (*67*). Specific enzymatic activity was expressed in mIU [nanomoles of 5-5′-dithiobis(2-nitrobenzoic acid) per minute per milligram of protein].

Oxygen consumption

The respiratory rate was measured using cells resuspended in respiratory buffer [0.5 mM EGTA, 3 mM $MgCl_2{\cdot}6H_2O$, 60 mM K-lactobionate, 20 mM taurine, 10 mM KH_2PO_4, 20 mM Hepes, 110 mM sucrose, and BSA (1 mg/ml) (pH 7.1)] and permeabilized by incubation with digitonin (15 µg per 10^6 cells). The respiratory rates of 3×10^6 to 5×10^6 cells were recorded at 37°C in 2-ml glass chambers using a high-resolution Oxygraph respirometer (Oroboros). Malate (5 mM) and pyruvate (5 mM) were added to provide NADH to complex I. The decarboxylation of pyruvate is catalyzed by pyruvate dehydrogenase (PDH), producing acetyl coenzyme A. Malate dehydrogenase (MDH) located in the mitochondrial matrix induces the oxidation of malate to oxaloacetate. The condensation of oxaloacetate and acetyl coenzyme A induces the formation of citrate by CS. Thus, the addition of malate and pyruvate results in the production of NADH by four enzymes: MDH, PDH, isocitrate dehydrogenase, and α-ketoglutarate dehydrogenase. Because of the activation of different malate shuttles, complex II is not activated. Citrate and α-ketoglutarate are depleted by antiport transport with malate. Thus, the addition of malate and pyruvate defines the respiration driven by complex I used to compensate the physiological proton leak. Activation of ATP synthesis was induced by the addition of 1.5 mM adenosine 5′-diphosphate (ADP). Thus, we obtained the respiration driven by complex I coupled to the ATP synthesis. The addition of succinate (10 mM) allowed reconstitution of TCA cycle function with the activation of succinate dehydrogenase. Thus, maximal respiration of the mitochondrial chain induced by the competition of the respiration driven by complexes I and II was determined. Addition of rotenone (10 µM)

inhibited the electron transfer from complex I to coenzyme Q and allowed the measurement of respiration driven by complex II. Oligomycin supplementation (8 μg/ml) inhibited the ATP synthesis, and respiration uncoupled driven by complex II was determined. Last, FCCP (1 μM) was added to test the quality of the permeabilization of the plasma membrane by digitonin.

Western blot analysis

Protein abundance was detected by immunoblot using commercially available antibodies and revealed using chemiluminescence. Frozen fibroblast pellets were lysed by a hypoosmotic shock (10 μl of H_2O per 10^6 cells). For coimmunoprecipitation, HEK293T pellets were mixed with 500 μl of lysis buffer consisting of 0.1 M NaCl, 1% Triton X-100, 1 mM phenylmethylsulfonyl fluoride (PMSF; Fluka), 1× SIGMAFAST protease inhibitor cocktail (Sigma-Aldrich), 5 mM EDTA, and 20 mM tris and rotated overnight at 4°C. The cellular protein content was determined with the BCA Kit.

Thirty micrograms of total fibroblasts or HEK293T-transfected protein was separated on SDS–polyacrylamide gel electrophoresis (PAGE) and transferred onto polyvinylidene difluoride membranes (Bio-Rad). Membranes were saturated with 5% nonfat milk dissolved in 0.1% tris-buffered saline (TBS)–Tween (pH 7.4, 137 mM NaCl, 2.7 mM KCl, 23 mM tris, and 0.1% Tween) for 1 hour at room temperature and incubated overnight at 4°C with polyclonal rabbit anti-WFS1 (1:500; Cell Signaling, USA), anti-MCU (1:1000; Abcam, UK), anti-MFN2 (1:1000; Cell Signaling), polyclonal chicken anti-NCS1 (1:1000; United States Biological, USA), monoclonal mouse anti-NDUFA13 (1:1000; Abcam), anti-SDHA (1:1000; Abcam), anti-UQCRC2 (1:1000; Abcam), anti-MTCO1 (1:1000; Abcam), anti–ATP synthase (1:1000; Invitrogen), anti-VDAC1 (1:1000; Abcam), anti-GAPDH (1:1000; Abcam), and anti-GRP75 (1:1000; Abcam). Anti-IP_3R antibody was a gift from J. Parys (Leuven, Belgium). Membranes were then washed three times in 0.1% TBS-Tween and incubated with anti-rabbit immunoglobulin G (IgG), anti-chicken IgG, or anti-mouse IgG horseradish peroxidase–linked antibody (1:10,000; Sigma-Aldrich) for 1 hour at room temperature. Immunoreactive proteins were visualized with enhanced chemiluminescence (ECL+ Western Blotting Detection Reagents, Amersham Biosciences, UK). Band intensities were quantified with ImageJ [National Institutes of Health (NIH), USA; http://rsb.info.nih.gov/ij].

In situ PLA

ER-mitochondria interactions were analyzed using an optimized in situ PLA targeting the IP_3R/GRP75/VDAC1 at the MAM interface, as previously described (*27*, *68*).

Yeast two-hybrid screening

Yeast two-hybrid screening was performed by Hybrigenics Services SAS, Paris, France (www.hybrigenics-services.com). The coding sequence for *Mus musculus*–Wfs1 (amino acids 1 to 311; GenBank accession number GI:28422738) was PCR amplified and cloned into pB29 as a C-terminal fusion to LexA (N-Wfs1-LexA-C). The construct was checked by sequencing the entire insert and used as a bait to screen a random-primed mouse inner ear cDNA library constructed into pP6. pB29 and pP6 derive from the original pBTM116 (*69*, *70*) and pGADGH (*71*) plasmids, respectively. Clones (54.3 million) (fivefold the complexity of the library) were screened using a mating approach with YHGX13 (Y187 ade2-101:loxP-kanMX-loxP, matα) and L40ΔGal4 (matα) yeast strains, as previously described (*72*). Twenty-nine His+ colonies were selected on a medium lacking tryptophan, leucine, and histidine. The prey fragments of the positive clones were amplified by PCR and sequenced at their 5′ and 3′ junctions. The resulting sequences were used to identify the corresponding interacting proteins in the GenBank database (National Center for Biotechnology Information) using a fully automated procedure. A confidence score [Predicted Biological Score (PBS)] was attributed to each interaction, as previously described (*73*).

The PBS relies on two different levels of analysis. First, a local score takes into account the redundancy and independency of prey fragments, as well as the distribution of reading frames and stop codons in overlapping fragments. Second, a global score takes into account the interactions found in all the screens performed at Hybrigenics using the same library. This global score represents the probability of an interaction being nonspecific. For practical purposes, the scores were divided into four categories, from A (highest confidence) to D (lowest confidence). A fifth category (E) specifically flags interactions involving highly connected prey domains previously found several times in screens performed on libraries derived from the same organism. Last, several of these highly connected domains have been confirmed as false positives of the technique and are now tagged as F. The PBS scores have been shown to positively correlate with the biological relevance of the interactions (*74*, *75*).

Confocal imaging

All confocal experiments were performed on fibroblasts placed on the stage of a Zeiss LSM 510 inverted confocal microscope (Zeiss, Le Pecq, France). Pericam-mt/pcDNA was used to measure $[Ca^{2+}]_m$. To measure cytosolic Ca^{2+}, fibroblasts were loaded with Fluo-4 AM (5 μM; Molecular Probes), Fluo-4 signal was obtained by excitation at 488 nm, and emitted light was collected at 515 nm. For pericam-mt, the excitation wavelength upon Ca^{2+} binding switches from 415 to 488 nm. Thus, the transfected cells were excited at 488, and images were collected at 515 nm. All the collected images were processed with ImageJ (NIH, USA; http://rsb.info.nih.gov/ij/). All confocal experiments were performed on fibroblasts placed on the stage of a Zeiss LSM 510 inverted confocal microscope (Zeiss) equipped with a 63× lens [oil immersion; numerical aperture (NA), 1.2].

ER Ca^{2+} release

Luminal Ca^{2+} dynamics were measured using the Ca^{2+}-sensitive FRET-based cameleon protein D1-ER (*76*). Cells were cultured on 24-mm coverslips and transfected with D1-ER. Cells were imaged on a Zeiss Axiovert 200M microscope, equipped with a 40× oil objective (NA, 1.3). Emission ratio imaging of D1-ER was accomplished by using a 436DF20 excitation filter, a 450-nm dichroic mirror, and two emission filters [475/40 for enhanced cyan fluorescent protein (ECFP) and 535/25 for citrine]. Exposure times were 100 ms, and images were taken every 1 to 2 s. The FRET signal (yellow fluorescent protein/CFP) was normalized to CFP emission intensity, and changes in ER Ca^{2+} were expressed as the ratio of the emissions at 535 and 470 nm. To induce Ca^{2+} release from ER, the cells were challenged with an agonist that, through interaction with G protein–coupled receptors, evokes a rapid discharge from IP_3Rs.

Ca^{2+} measurements with aequorin constructs

For mt-AEQ measurements, coverslips with control and mutated fibroblasts overexpressing MCU were incubated for 2 hours in KRB (Krebs-Ringer modified buffer) (135 mM NaCl, 5 mM KCl, 0.4 mM

KH_2PO_4, 1 mM $MgSO_4$, 5.5 mM glucose, and 20 mM Hepes (pH 7.4)] at 37°C supplemented with wild-type coelenterazine (5 M) and then transferred to the perfusion chamber. In the experiments with permeabilized cells, cells were perfused in intracellular buffer [140 mM KCl, 10 mM NaCl, 1 mM KH_2PO_4, 5.5 mM glucose, 2 mM $MgSO_4$, 1 mM ATP, 2 mM Na^+ succinate, and 20 mM Hepes (pH 7.05)] at 37°C. Cells were permeabilized through a 1-min perfusion with 100 μM digitonin during luminescence measurements. After a 2-min washing (to remove digitonin), $[Ca^{2+}]_m$ uptake was estimated by mt-AEQ after cell perfusion with the same intracellular solution without EGTA and containing Ca^{2+} at different concentrations (1 and 4 μM). Calcium uptake speed was calculated as the first derivative by using the first derivative function smoothed for three time points.

To reconstitute erAEQ with high efficiency, luminal $[Ca^{2+}]$ of the ER was first reduced by incubating the cells for 45 min at 4°C in KRB supplemented with 5 μM coelenterazine, the Ca^{2+} ionophore ionomycin, and 600 μM EGTA. After incubation, the cells were extensively washed with KRB supplemented with 2% BSA and 2 mM EGTA before the luminescence measurement was initiated. Aequorin signals were measured in KRB supplemented with either 1 mM $CaCl_2$ or 100 μM EGTA, using a purpose-built luminometer. The agonist (bradykinin at 100 μM) was added to the same medium.

Mitochondrial membrane potential

To measure $\Delta\psi_m$, fibroblasts were loaded with 10 nM TMRM (Life Technologies) for 20 min at 37°C, followed by washout. TMRM dyes were excited at 565 nm, and emitted light was collected at 585 nm. At the end of each experiment using TMRM dyes, cells were exposed to the mitochondrial uncoupler FCCP (1 μM) to fully dissipate ($\Delta\psi_m$) and to determine the dynamic range of the dye. TMRM fluorescence was normalized to the fluorescence signals obtained after FCCP application. After loading, cells were placed on the stage of a Zeiss LSM 510 inverted confocal microscope (Zeiss) equipped with a 63× lens (oil immersion; NA, 1.2). Collected images were processed with ImageJ (NIH, USA; http://rsb.info.nih.gov/ij/). Detection of $\Delta\psi_m$ was also performed by loading cells with a JC-1 staining kit (Thermo Fisher Scientific). JC-1 emissions were collected using a Zeiss LSM 510 confocal microscope equipped with a 40× oil objective (NA, 1.30). The green fluorescent/red fluorescent intensity ratios (540/595 nm) were calculated to determine $\Delta\psi_m$ levels.

Coimmunoprecipitation

pcDNA-IP_3R1 was provided by K. Mikoshiba (Okasaki, Japan) (*77*). The plasmid expressing Wfs1 was obtained by subcloning Wfs1 into myc-tagged pCS2 + MT using Hind III and Bam H1. Ncs1 was subcloned into C-terminal p3XFLAG-CMV between Eco R1 and Bam H1. To assess interactions between IP_3R1 and Ncs1-Flag and between Wfs1-myc and Ncs1-Flag, 100 μg of proteins from each transfection reaction was mixed with 2 μl of mouse anti-Flag M2 antibody (Sigma-Aldrich) containing 1 mM PMSF and 2% BSA in DWBa buffer [100 mM NaCl, 20 mM tris, 1 mM EDTA (pH 7.4), 1% Triton X-100]. For IP_3R1 and Wfs1-myc antibody, 100 μg of proteins from each transfection reaction was mixed with 2 μg of a rabbit anti-myc (Sigma-Aldrich). The mixtures were vortexed and incubated at 4°C overnight. Thirty microliters of Sepharose A and 10 μl of Sepharose G (Immunoprecipitation Starter Pack, GE Healthcare) were used per sample and prepared following supplier instruction. Sepharose suspension was added to the tubes containing antibody/protein samples and mixed on a rotating wheel at 4°C for 1 hour. The samples were then centrifuged at 2000 rpm for 1 min and washed three times with 1 ml of DWBa and two times with 1 ml of DWBb [100 mM NaCl, 20 mM tris, and 1 mM EDTA (pH 7.4)] each. The pellets obtained after the last wash were resuspended in 25 μl of Laemmli sample buffer (Bio-Rad). Last, all the samples were boiled at 95°C for 5 min and centrifuged at 13,200 rpm for 1 min. The supernatants were loaded on an SDS-PAGE gel for Western blotting and analyzed with an anti-myc antibody for Wfs1-myc and Ncs1-Flag coimmunoprecipitation, with the rabbit Rbt476 pan anti-IP_3R antibody (a gift from J. Parys, Leuven, Belgium) (*78*) for Ncs1-Flag and IP_3R1 coimmunoprecipitation and Wfs1-myc and IP_3R1 coimmunoprecipitation. Thirty micrograms of protein from Ncs1-Flag and Wfs1-myc transfection reactions was used as controls.

Transmission electron microscopy

Cells were immersed in a solution of 2.5% glutaraldehyde in PHEM buffer (1×, pH 7.4) overnight at 4°C, rinsed in PHEM buffer, and postfixed in a 0.5% osmic acid for 2 hours in the dark and at room temperature. After two rinses in PHEM buffer, cells were dehydrated in a graded series of ethanol solutions (30 to 100%) and were embedded in EMbed 812 using an Automated Microwave Tissue Processor for Electronic Microscopy (Leica). Ultrathin sections (70 nm; Leica-Reichert Ultracut E) were collected at different levels of each block. These sections were stained with uranyl acetate and lead citrate before examination in a Tecnai F20 TEM at 200 kV in the CoMET Montpellier Rio Imaging (MRI) facilities, Institute for Neurosciences of Montpellier, France. To evaluate the frequency of contact between the mitochondria and the ER in the different fibroblasts, we randomly took 20 images of cytoplasmic area from 20 different cells in each sample with a JEOL 1400 TEM at ×15,000 magnification. In each image, we counted the number of mitochondria (403 in control cells and 649 in patient cells for a total of 1052 mitochondria) and calculated the proportion of mitochondria in close contact with ER (<30 nm). Moreover, the perimeter of each mitochondria and the proportion of the mitochondrial surface closely associated with ER were calculated. For experiments with knockdown of NCS1, 257 mitochondria were analyzed for siScr and 239 mitochondria were analyzed for siRNA NCS1.

Statistical analysis

The Mann-Whitney was used to compare the fibroblasts from WFS1 patients and controls. The Kruskal-Wallis test was used to compare the effect of the overexpression of NCS1 or vector alone. Differences were considered significant at $^*P < 0.05$, $^{**}P < 0.01$, and $^{***}P < 0.001$. Proportions of ER-mitochondrial contacts between controls and patient fibroblasts were compared with their 95% confidence intervals.

SUPPLEMENTARY MATERIALS

www.sciencesignaling.org/cgi/content/full/11/553/eaaq1380/DC1

Fig. S1. WFS1 interacts with IP_3R.
Fig. S2. Ca^{2+} imaging in thapsigargin-treated cells.
Fig. S3. Analysis of mitochondrial respiratory rate.
Fig. S4. NCS1 interacts with WFS1 and IP_3R.
Fig. S5. Time course of siRNA-mediated knockdown of WFS1.
Fig. S6. Time course of siRNA-mediated knockdown of NCS1.
Fig. S7. Representative cytosolic and $[Ca^{2+}]_m$ in control and patient fibroblasts expressing Flag or NCS1-Flag.
Fig. S8. Mitochondrial protein abundance in patient fibroblasts overexpressing NCS1.

Table S1. Clinical features of control subjects and patients with Wolfram syndrome.
Table S2. TEM image analysis results.
Table S3. Two-hybrid screening results.

REFERENCES AND NOTES

1. A. Bononi, S. Missiroli, F. Poletti, J. M. Suski, C. Agnoletto, M. Bonora, E. De Marchi, C. Giorgi, S. Marchi, S. Patergnani, A. Rimessi, M. R. Wieckowski, P. Pinton, Mitochondria-associated membranes (MAMs) as hotspot Ca^{2+} signaling units. *Adv. Exp. Med. Biol.* **740**, 411–437 (2012).
2. G. Csordás, C. Renken, P. Várnai, L. Walter, D. Weaver, K. F. Buttle, T. Balla, C. A. Mannella, G. Hajnóczky, Structural and functional features and significance of the physical linkage between ER and mitochondria. *J. Cell Biol.* **174**, 915–921 (2006).
3. S. Marchi, S. Patergnani, P. Pinton, The endoplasmic reticulum–mitochondria connection: One touch, multiple functions. *Biochim. Biophys. Acta* **1837**, 461–469 (2014).
4. C. Giorgi, S. Missiroli, S. Patergnani, J. Duszynski, M. R. Wieckowski, P. Pinton, Mitochondria-associated membranes: Composition, molecular mechanisms, and physiopathological implications. *Antioxid. Redox Signal.* **22**, 995–1019 (2015).
5. G. Hajnöczky, G. Csordás, S. Das, C. Garcia-Perez, M. Saotome, S. Sinha Roy, M. Yi, Mitochondrial calcium signalling and cell death: Approaches for assessing the role of mitochondrial Ca^{2+} uptake in apoptosis. *Cell Calcium* **40**, 553–560 (2006).
6. A. U. Joshi, O. S. Kornfeld, D. Mochly-Rosen, The entangled ER-mitochondrial axis as a potential therapeutic strategy in neurodegeneration: A tangled duo unchained. *Cell Calcium* **60**, 218–234 (2016).
7. M. Krols, G. van Isterdael, B. Asselbergh, A. Kremer, S. Lippens, V. Timmerman, S. Janssens, Mitochondria-associated membranes as hubs for neurodegeneration. *Acta Neuropathol.* **131**, 505–523 (2016).
8. T. G. Barrett, S. E. Bundey, A. F. Macleod, Neurodegeneration and diabetes: UK nationwide study of Wolfram (DIDMOAD) syndrome. *Lancet* **346**, 1458–1463 (1995).
9. S. Bundey, A. R. Fielder, K. Poulton, Wolfram syndrome: Mitochondrial disorder. *Lancet* **342**, 1059–1060 (1993).
10. K. Takeda, H. Inoue, Y. Tanizawa, Y. Matsuzaki, J. Oba, Y. Watanabe, K. Shinoda, Y. Oka, WFS1 (Wolfram syndrome 1) gene product: Predominant subcellular localization to endoplasmic reticulum in cultured cells and neuronal expression in rat brain. *Hum. Mol. Genet.* **10**, 477–484 (2001).
11. M. Cagalinec, M. Liiv, Z. Hodurova, M. A. Hickey, A. Vaarmann, M. Mandel, A. Zeb, V. Choubey, M. Kuum, D. Safiulina, E. Vasar, V. Veksler, A. Kaasik, Role of mitochondrial dynamics in neuronal development: Mechanism for Wolfram syndrome. *PLOS Biol.* **14**, e1002511 (2016).
12. S. Hofmann, C. Philbrook, K.-D. Gerbitz, M. F. Bauer, Wolfram syndrome: Structural and functional analyses of mutant and wild-type wolframin, the *WFS1* gene product. *Hum. Mol. Genet.* **12**, 2003–2012 (2003).
13. S. Hofmann, M. F. Bauer, Wolfram syndrome-associated mutations lead to instability and proteasomal degradation of wolframin. *FEBS Lett.* **580**, 4000–4004 (2006).
14. M. Akiyama, M. Hatanaka, Y. Ohta, K. Ueda, A. Yanai, Y. Uehara, K. Tanabe, M. Tsuru, M. Miyazaki, S. Saeki, T. Saito, K. Shinoda, Y. Oka, Y. Tanizawa, Increased insulin demand promotes while pioglitazone prevents pancreatic beta cell apoptosis in *Wfs1* knockout mice. *Diabetologia* **52**, 653–663 (2009).
15. S. E. Wiley, A. Y. Andreyev, A. S. Divakaruni, R. Karisch, G. Perkins, E. A. Wall, P. van der Geer, Y.-F. Chen, T.-F. Tsai, M. I. Simon, B. G. Neel, J. E. Dixon, A. N. Murphy, Wolfram syndrome protein, Miner1, regulates sulphydryl redox status, the unfolded protein response, and Ca^{2+} homeostasis. *EMBO Mol. Med.* **5**, 904–918 (2013).
16. A. A. Osman, M. Saito, C. Makepeace, M. A. Permutt, P. Schlesinger, M. Mueckler, Wolframin expression induces novel ion channel activity in endoplasmic reticulum membranes and increases intracellular calcium. *J. Biol. Chem.* **278**, 52755–52762 (2003).
17. D. Takei, H. Ishihara, S. Yamaguchi, T. Yamada, A. Tamura, H. Katagiri, Y. Maruyama, Y. Oka, WFS1 protein modulates the free Ca^{2+} concentration in the endoplasmic reticulum. *FEBS Lett.* **580**, 5635–5640 (2006).
18. M. Zatyka, G. Da Silva Xavier, E. A. Bellomo, W. Leadbeater, D. Astuti, J. Smith, F. Michelangeli, G. A. Rutter, T. G. Barrett, Sarco(endo)plasmic reticulum ATPase is a molecular partner of Wolfram syndrome 1 protein, which negatively regulates its expression. *Hum. Mol. Genet.* **24**, 814–827 (2014).
19. M. Bonora, C. Giorgi, A. Bononi, S. Marchi, S. Patergnani, A. Rimessi, R. Rizzuto, P. Pinton, Subcellular calcium measurements in mammalian cells using jellyfish photoprotein aequorin-based probes. *Nat. Protoc.* **8**, 2105–2118 (2013).
20. C. Giorgi, M. Bonora, G. Sorrentino, S. Missiroli, F. Poletti, J. M. Suski, F. G. Ramirez, R. Rizzuto, F. Di Virgilio, E. Zito, P. P. Pandolfi, M. R. Wieckowski, F. Mammano, G. Del Sal, P. Pinton, p53 at the endoplasmic reticulum regulates apoptosis in a Ca^{2+}-dependent manner. *Proc. Natl. Acad. Sci. U.S.A.* **112**, 1779–1784 (2015).
21. A. Rueda, L. García, L.-E. Soria-Jasso, J.-A. Arias-Montaño, A. Guerrero-Hernández, The initial inositol 1,4,5-trisphosphate response induced by histamine is strongly amplified by Ca^{2+} release from internal stores in smooth muscle. *Cell Calcium* **31**, 161–173 (2002).
22. J. E. Vance, MAM (mitochondria-associated membranes) in mammalian cells: Lipids and beyond. *Biochim. Biophys. Acta* **1841**, 595–609 (2014).
23. A. R. van Vliet, T. Verfaillie, P. Agostinis, New functions of mitochondria associated membranes in cellular signaling. *Biochim. Biophys. Acta* **1843**, 2253–2262 (2014).
24. S. Patergnani, J. M. Suski, C. Agnoletto, A. Bononi, M. Bonora, E. De Marchi, C. Giorgi, S. Marchi, S. Missiroli, F. Poletti, A. Rimessi, J. Duszynski, M. R. Wieckowski, P. Pinton, Calcium signaling around mitochondria associated membranes (MAMs). *Cell Commun. Signal.* **9**, 19 (2011).
25. S. Grimm, The ER–mitochondria interface: The social network of cell death. *Biochim. Biophys. Acta* **1823**, 327–334 (2012).
26. G. Szabadkai, K. Bianchi, P. Várnai, D. De Stefani, M. R. Wieckowski, D. Cavagna, A. I. Nagy, T. Balla, R. Rizzuto, Chaperone-mediated coupling of endoplasmic reticulum and mitochondrial Ca^{2+} channels. *J. Cell Biol.* **175**, 901–911 (2006).
27. E. Tubbs, P. Theurey, G. Vial, N. Bendridi, A. Bravard, M.-A. Chauvin, J. Ji-Cao, F. Zoulim, B. Bartosch, M. Ovize, H. Vidal, J. Rieusset, Mitochondria-associated endoplasmic reticulum membrane (MAM) integrity is required for insulin signaling and is implicated in hepatic insulin resistance. *Diabetes* **63**, 3279–3294 (2014).
28. O. M. de Brito, L. Scorrano, Mitofusin 2 tethers endoplasmic reticulum to mitochondria. *Nature* **456**, 605–610 (2008).
29. O. Pongs, J. Lindemeier, X. R. Zhu, T. Theil, D. Engelkamp, I. Krah-Jentgens, H.-G. Lambrecht, K. W. Koch, J. Schwemer, R. Rivosecchi, A. Mallart, J. Galceran, I. Canal, J. A. Barbas, A. Ferrús, Frequenin—A novel calcium-binding protein that modulates synaptic efficacy in the Drosophila nervous system. *Neuron* **11**, 15–28 (1993).
30. S. Nakao, S. Wakabayashi, T. Y. Nakamura, Stimulus-dependent regulation of nuclear Ca^{2+} signaling in cardiomyocytes: A role of neuronal calcium sensor-1. *PLOS ONE* **10**, e0125050 (2015).
31. C. Schlecker, W. Boehmerle, A. Jeromin, B. DeGray, A. Varshney, Y. Sharma, K. Szigeti-Buck, B. E. Ehrlich, Neuronal calcium sensor-1 enhancement of InsP3 receptor activity is inhibited by therapeutic levels of lithium. *J. Clin. Invest.* **116**, 1668–1674 (2006).
32. S. X. Zhang, E. Sanders, S. J. Fliesler, J. J. Wang, Endoplasmic reticulum stress and the unfolded protein responses in retinal degeneration. *Exp. Eye Res.* **125**, 30–40 (2014).
33. N. Kabbani, L. Negyessy, R. Lin, P. Goldman-Rakic, R. Levenson, Interaction with neuronal calcium sensor NCS-1 mediates desensitization of the D2 dopamine receptor. *J. Neurosci.* **22**, 8476–8486 (2002).
34. S. G. Fonseca, S. Ishigaki, C. M. Oslowski, S. Lu, K. L. Lipson, R. Ghosh, E. Hayashi, H. Ishihara, Y. Oka, M. Alan Permutt, F. Urano, Wolfram syndrome 1 gene negatively regulates ER stress signaling in rodent and human cells. *J. Clin. Invest.* **120**, 744–755 (2010).
35. S. M. Horner, C. Wilkins, S. Badil, J. Iskarpatyoti, M. Gale Jr., Proteomic analysis of mitochondrial-associated ER membranes (MAM) during RNA virus infection reveals dynamic changes in protein and organelle trafficking. *PLOS ONE* **10**, e0117963 (2015).
36. C. N. Poston, S. C. Krishnan, C. R. Bazemore-Walker, In-depth proteomic analysis of mammalian mitochondria-associated membranes (MAM). *J. Proteomics* **79**, 219–230 (2013).
37. A. Zhang, C. D. Williamson, D. S. Wong, M. D. Bullough, K. J. Brown, Y. Hathout, A. M. Colberg-Poley, Quantitative proteomic analyses of human cytomegalovirus-induced restructuring of endoplasmic reticulum-mitochondrial contacts at late times of infection. *Mol. Cell. Proteomics* **10**, M111.009936 (2011).
38. J. A. Petko, N. Kabbani, C. Frey, M. Woll, K. Hickey, M. Craig, V. A. Canfield, R. Levenson, Proteomic and functional analysis of NCS-1 binding proteins reveals novel signaling pathways required for inner ear development in zebrafish. *BMC Neurosci.* **10**, 27 (2009).
39. R. D. Burgoyne, J. L. Weiss, The neuronal calcium sensor family of Ca^{2+}-binding proteins. *Biochem. J.* **353**, 1–12 (2001).
40. D. Naon, M. Zaninello, M. Giacomello, T. Varanita, F. Grespi, S. Lakshminaranayan, A. Serafini, M. Semenzato, S. Herkenne, M. I. Hernández-Alvarez, A. Zorzano, D. De Stefani, G. W. Dorn II, L. Scorrano, Critical reappraisal confirms that Mitofusin 2 is an endoplasmic reticulum–mitochondria tether. *Proc. Natl. Acad. Sci. U.S.A.* **113**, 11249–11254 (2016).
41. C.-H. Wang, Y.-F. Chen, C.-Y. Wu, P.-C. Wu, Y.-L. Huang, C.-H. Kao, C.-H. Lin, L.-S. Kao, T.-F. Tsai, Y.-H. Wei, Cisd2 modulates the differentiation and functioning of adipocytes by regulating intracellular Ca^{2+} homeostasis. *Hum. Mol. Genet.* **23**, 4770–4785 (2014).
42. C.-H. Wang, Y.-H. Wei, Role of mitochondrial dysfunction and dysregulation of Ca^{2+} homeostasis in the pathophysiology of insulin resistance and type 2 diabetes. *J. Biomed. Sci.* **24**, 70 (2017).
43. S. Paillusson, R. Stoica, P. Gomez-Suaga, D. H. W. Lau, S. Mueller, T. Miller, C. C. J. Miller, There's something wrong with my MAM; the ER–mitochondria axis and neurodegenerative diseases. *Trends Neurosci.* **39**, 146–157 (2016).
44. E. Area-Gomez, E. A. Schon, Mitochondria-associated ER membranes and Alzheimer disease. *Curr. Opin. Genet. Dev.* **38**, 90–96 (2016).

45. S. Watanabe, H. Ilieva, H. Tamada, H. Nomura, O. Komine, F. Endo, S. Jin, P. Mancias, H. Kiyama, K. Yamanaka, Mitochondria-associated membrane collapse is a common pathomechanism in *SIGMAR1*- and *SOD1*-linked ALS. *EMBO Mol. Med.* **8**, 1421–1437 (2016).
46. T. Y. Nakamura, S. Nakao, S. Wakabayashi, Neuronal Ca^{2+} sensor-1 contributes to stress tolerance in cardiomyocytes via activation of mitochondrial detoxification pathways. *J. Mol. Cell. Cardiol.* **99**, 23–34 (2016).
47. J. B. Hilson, S. N. Merchant, J. C. Adams, J. T. Joseph, Wolfram syndrome: A clinicopathologic correlation. *Acta Neuropathol.* **118**, 415–428 (2009).
48. J. Gromada, C. Bark, K. Smidt, A. M. Efanov, J. Janson, S. A. Mandic, D.-L. Webb, W. Zhang, B. Meister, A. Jeromin, P.-O. Berggren, Neuronal calcium sensor-1 potentiates glucose-dependent exocytosis in pancreatic β cells through activation of phosphatidylinositol 4-kinase β. *Proc. Natl. Acad. Sci. U.S.A.* **102**, 10303–10308 (2005).
49. A. J. Reynolds, S. E. Bartlett, C. Morgans, The distribution of neuronal calcium sensor-1 protein in the developing and adult rat retina. *Neuroreport* **12**, 725–728 (2001).
50. M. Zatyka, G. Da Silva Xavier, E. A. Bellomo, W. Leadbeater, D. Astuti, J. Smith, F. Michelangeli, G. A. Rutter, T. G. Barrett, Sarco(endo)plasmic reticulum ATPase is a molecular partner of Wolfram syndrome 1 protein, which negatively regulates its expression. *Hum. Mol. Genet.* **24**, 814–827 (2015).
51. D.-Y. Yu, S. J. Cringle, C. Balaratnasingam, W. H. Morgan, P. K. Yu, E.-N. Su, Retinal ganglion cells: Energetics, compartmentation, axonal transport, cytoskeletons and vulnerability. *Prog. Retin. Eye Res.* **36**, 217–246 (2013).
52. C. Y. Yu Wai Man, P. F. Chinnery, P. G. Griffiths, Optic neuropathies—Importance of spatial distribution of mitochondria as well as function. *Med. Hypotheses* **65**, 1038–1042 (2005).
53. M. Levy, G. C. Faas, P. Saggau, W. J. Craigen, J. D. Sweatt, Mitochondrial regulation of synaptic plasticity in the hippocampus. *J. Biol. Chem.* **278**, 17727–17734 (2003).
54. Z.-H. Sheng, Q. Cai, Mitochondrial transport in neurons: Impact on synaptic homeostasis and neurodegeneration. *Nat. Rev. Neurosci.* **13**, 77–93 (2012).
55. M.-Y. Lin, Z.-H. Sheng, Regulation of mitochondrial transport in neurons. *Exp. Cell Res.* **334**, 35–44 (2015).
56. R. G. Swift, D. B. Sadler, M. Swift, Psychiatric findings in Wolfram syndrome homozygotes. *Lancet* **336**, 667–669 (1990).
57. A. N. Bischoff, A. M. Reiersen, A. Buttlaire, A. Al-Iozi, T. Doty, B. A. Marshall, T. Hershey; Washington University Wolfram Syndrome Research Group, Selective cognitive and psychiatric manifestations in Wolfram syndrome. *Orphanet J. Rare Dis.* **10**, 66 (2015).
58. P. Shrestha, A. Mousa, N. Heintz, Layer 2/3 pyramidal cells in the medial prefrontal cortex moderate stress induced depressive behaviors. *eLife* **4**, e08752 (2015).
59. J. Xavier, N. Bourvis, A. Tanet, T. Ramos, D. Perisse, I. Marey, D. Cohen, A. Consoli, Bipolar disorder type 1 in a 17-year-old girl with Wolfram syndrome. *J. Child Adolesc. Psychopharmacol.* **26**, 750–755 (2016).
60. V. B. de Rezende, D. V. Rosa, C. M. Comim, L. A. V. Magno, A. L. S. Rodrigues, P Vidigal, A. Jeromin, J. Quevedo, M. A. Romano-Silva, NCS-1 deficiency causes anxiety and depressive-like behavior with impaired non-aversive memory in mice. *Physiol. Behav.* **130**, 91–98 (2014).
61. P. O. Koh, A. S. Undie, N. Kabbani, R. Levenson, P. S. Goldman-Rakic, M. S. Lidow, Up-regulation of neuronal calcium sensor-1 (NCS-1) in the prefrontal cortex of schizophrenic and bipolar patients. *Proc. Natl. Acad. Sci. U.S.A.* **100**, 313–317 (2003).
62. C. Angebault, N. Gueguen, V. Desquiret-Dumas, A. Chevrollier, V. Guillet, C. Verny, J. Cassereau, M. Ferre, D. Milea, P. Amati-Bonneau, D. Bonneau, V. Procaccio, Pascal Reynier, D. Loiseau, Idebenone increases mitochondrial complex I activity in fibroblasts from LHON patients while producing contradictory effects on respiration. *BMC Res. Notes* **4**, 557 (2011).
63. D. Loiseau, A. Chevrollier, C. Verny, V. Guillet, N. Gueguen, M. A. Pou de Crescenzo, M. Ferré, M. C. Malinge, A. Guichet, G. Nicolas, P. Amati-Bonneau, Y. Malthièry, D. Bonneau, P. Reynier, Mitochondrial coupling defect in Charcot–Marie–Tooth type 2A disease. *Ann. Neurol.* **61**, 315–323 (2007).
64. P. Bénit, A. Slama, P. Rustin, Decylubiquinol impedes mitochondrial respiratory chain complex I activity. *Mol. Cell. Biochem.* **314**, 45–50 (2008).
65. A. M. James, Y.-H. Wei, C.-Y. Pang, M. P. Murphy, Altered mitochondrial function in fibroblasts containing MELAS or MERRF mitochondrial DNA mutations. *Biochem. J.* **318** (Pt. 2), 401–407 (1996).
66. P. Rustin, D. Chretien, T. Bourgeron, A. Wucher, J. M. Saudubray, A. Rotig, A. Munnich, Assessment of the mitochondrial respiratory chain. *Lancet* **338**, 60 (1991).
67. J. D. Schulman, J. P. Blass, Measurement of citrate synthase activity in human fibroblasts. *Clin. Chim. Acta* **33**, 467–469 (1971).
68. P. Theurey, E. Tubbs, G. Vial, J. Jacquemetton, N. Bendridi, M.-A. Chauvin, M. R. Alam, M. Le Romancer, H. Vidal, J. Rieusset, Mitochondria-associated endoplasmic reticulum membranes allow adaptation of mitochondrial metabolism to glucose availability in the liver. *J. Mol. Cell Biol.* **8**, 129–149 (2016).
69. A. B. Vojtek, S. M. Hollenberg, Ras-Raf interaction: Two-hybrid analysis. *Methods Enzymol.* **255**, 331–342 (1995).
70. F. Béranger, S. Aresta, J. de Gunzburg, J. Camonis, Getting more from the two-hybrid system: N-terminal fusions to LexA are efficient and sensitive baits for two-hybrid studies. *Nucleic Acids Res.* **25**, 2035–2036 (1997).
71. P. Bartel, C. T. Chien, R. Sternglanz, S. Fields, Elimination of false positives that arise in using the two-hybrid system. *Biotechniques* **14**, 920–924 (1993).
72. M. Fromont-Racine, J.-C. Rain, P. Legrain, Toward a functional analysis of the yeast genome through exhaustive two-hybrid screens. *Nat. Genet.* **16**, 277–282 (1997).
73. E. Formstecher, S. Aresta, V. Collura, A. Hamburger, A. Meil, A. Trehin, C. Reverdy, V. Betin, S. Maire, C. Brun, B. Jacq, M. Arpin, Y. Bellaiche, S. Bellusci, P. Benaroch, M. Bornens, R. Chanet, P. Chavrier, O. Delattre, V. Doye, R. Fehon, G. Faye, T. Galli, J.-A. Girault, B. Goud, J. de Gunzburg, L. Johannes, M.-P. Junier, V. Mirouse, A. Mukherjee, D. Papadopoulo, F. Perez, A. Plessis, C. Rossé, S. Saule, D. Stoppa-Lyonnet, A. Vincent, M. White, P. Legrain, J. Wojcik, J. Camonis, L. Daviet, Protein interaction mapping: A *Drosophila* case study. *Genome Res.* **15**, 376–384 (2005).
74. J.-C. Rain, L. Selig, H. De Reuse, V. Battaglia, C. Reverdy, S. Simon, G. Lenzen, F. Petel, J. Wojcik, V. Schächter, Y. Chemama, A. Labigne, P. Legrain, The protein–protein interaction map of *Helicobacter pylori*. *Nature* **409**, 211–215 (2001).
75. J. Wojcik, I. G. Boneca, P. Legrain, Prediction, assessment and validation of protein interaction maps in bacteria. *J. Mol. Biol.* **323**, 763–770 (2002).
76. R. Rudolf, M. Mongillo, R. Rizzuto, T. Pozzan, Looking forward to seeing calcium. *Nat. Rev. Mol. Cell Biol.* **4**, 579–586 (2003).
77. T. Furuichi, S. Yoshikawa, A. Miyawaki, K. Wada, N. Maeda, K. Mikoshiba, Primary structure and functional expression of the inositol 1,4,5-trisphosphate-binding protein P_{400}. *Nature* **342**, 32–38 (1989).
78. G. Bultynck, K. Szlufcik, N. N. Kasri, Z. Assefa, G. Callewaert, L. Missiaen, J. B. Parys, H. De Smedt, Thimerosal stimulates Ca^{2+} flux through inositol 1,4,5-trisphosphate receptor type 1, but not type 3, via modulation of an isoform-specific Ca^{2+}-dependent intramolecular interaction. *Biochem. J.* **381**, 87–96 (2004).

Acknowledgments: We thank the patients and their families for their contribution to the clinical studies. We are indebted to the MRI for their technical support. We thank J. Parys for providing the pan IP_3R Rbt476 antibody, K. Mikoshiba for providing the IP_3R1 pcDNA vector, and N. Bendridi and M.-A. Chauvin for technical assistance. We thank A. Miyawaki who gifted us with the ratiometric pericam-mt plasmid. We thank V. Paquis-Flucklinger, C. Rouzier, and A. Chaussenot for their contributions. We thank P. Carroll for his contribution in reading the manuscript. We thank S. Cubaynes for help with statistics. **Funding:** We are indebted to the INSERM and Université Montpellier for providing institutional support and to the patient associations Union National des Aveugles et Déficients Visuels (UNADEV) and Association Syndrome de Wolfram for their financial support. This work was supported by grants from the Agence Nationale pour la Recherche (ANR-12-JSV1-0008-01), Fondation pour la Recherche Médicale, and Fondation de France. C.A. was supported by the Fondation de France. **Author contributions:** C.A. performed most of the experiments, analyzed the data, and contributed to writing the manuscript. J.F. performed Ca^{2+} imaging and wrote the paper. S.P. and A.D. performed aequorin experiments. J.R. performed in situ PLA and mitochondrial content quantification. C.A.A. and J.K. carried out coimmunoprecipitation experiments. J.J., C.M., M.Q., and D.B.-W. helped in the characterization of cells. C.C. and M.T. performed TEM. D.M. and C.H. provided reagents. P.P. analyzed data. A.L. provided reagents and analyzed the data. B.D. and C.D. conceived and designed the study, analyzed the data, and wrote the paper. **Competing interests:** The authors declare that they have no competing interests. **Data and materials availability:** All data needed to evaluate the conclusions in the paper are present in the paper or the Supplementary Materials.

Submitted 5 October 2017
Accepted 4 October 2018
Published 23 October 2018
10.1126/scisignal.aaq1380

Citation: C. Angebault, J. Fauconnier, S. Patergnani, J. Rieusset, A. Danese, C. A. Affortit, J. Jagodzinska, C. Mégy, M. Quiles, C. Cazevieille, J. Korchagina, D. Bonnet-Wersinger, D. Milea, C. Hamel, P. Pinton, M. Thiry, A. Lacampagne, B. Delprat, C. Delettre, ER-mitochondria cross-talk is regulated by the Ca^{2+} sensor NCS1 and is impaired in Wolfram syndrome. *Sci. Signal.* **11**, eaaq1380 (2018).

Science Signaling

ER-mitochondria cross-talk is regulated by the Ca^{2+} sensor NCS1 and is impaired in Wolfram syndrome

Claire Angebault, Jérémy Fauconnier, Simone Patergnani, Jennifer Rieusset, Alberto Danese, Corentin A. Affortit, Jolanta Jagodzinska, Camille Mégy, Mélanie Quiles, Chantal Cazevieille, Julia Korchagina, Delphine Bonnet-Wersinger, Dan Milea, Christian Hamel, Paolo Pinton, Marc Thiry, Alain Lacampagne, Benjamin Delprat and Cécile Delettre

Sci. Signal. **11** (553), eaaq1380.
DOI: 10.1126/scisignal.aaq1380

The ER-mitochondria connection for Ca^{2+}

Loss-of-function mutations in the ER protein WFS1 result in Wolfram syndrome; however, some of the defining symptoms of this disorder, such as diabetes and optic atrophy, are due to mitochondrial dysfunction. Using fibroblasts from Wolfram syndrome patients or normal individuals, Angebault *et al*. found that WFS1 deficiency was associated with decreased Ca^{2+} uptake by mitochondria, reduced mitochondrial contact with the ER, and decreased mitochondrial respiration. WFS1 interacted with a Ca^{2+}-sensing protein, called NCS1, and NCS1 abundance was lower in patient fibroblasts than in control fibroblasts. Reconstituting NCS1 in patient fibroblasts restored mitochondrial respiration and Ca^{2+} signaling dynamics. These results explain how a deficiency in an ER protein impairs mitochondrial activity and suggest that defective ER-mitochondria association may contribute to the pathogenesis of neurodegenerative disorders.